

Article

Adaptive Position Control for Two-Mass Drives with Nonlinear Flexible Joints

Marcin Jastrzębski , Jacek Kabziński  and Przemysław Mosiołek * 

Institute of Automatic Control, Lodz University of Technology, 90-537 Łódź, Poland; marcin.jastrzebski@p.lodz.pl (M.J.); jacek.kabzinski@p.lodz.pl (J.K.)

* Correspondence: przemyslaw.mosiolek@p.lodz.pl

Abstract: We consider a two-mass drive with a flexible joint with a nonlinear characteristic of the transmitted torque as a function of the torsion angle. We propose a new, nonlinear, adaptive position-tracking controller, taking this nonlinearity of stiffness into account. The derivation of the controller is based on nonlinear adaptive control theory, incorporates several non-standard mathematical techniques and provides a proof of the uniform ultimate boundedness of tracking errors. As the result, we present a controller that solves the position tracking problem, attenuates dangerous torsional oscillations in the shaft and operates correctly in the presence of unknown torques acting on both sides of the joint, even if all plant parameters are unknown. We demonstrate experimentally that using some materials indeed introduces a nonlinear characteristic of the joint. We prove via real plant experiments that the proposed control algorithm is easily implementable with a DSP controller in real-world applications.

Keywords: two-mass drive; flexible joint; nonlinear adaptive control



Citation: Jastrzębski, M.; Kabziński, J.; Mosiołek, P. Adaptive Position Control for Two-Mass Drives with Nonlinear Flexible Joints. *Energies* **2024**, *17*, 425. <https://doi.org/10.3390/en17020425>

Academic Editor: Youguang Guo

Received: 18 December 2023

Revised: 8 January 2024

Accepted: 10 January 2024

Published: 15 January 2024



Copyright: © 2024 by the authors. Licensee MDPI, Basel, Switzerland. This article is an open access article distributed under the terms and conditions of the Creative Commons Attribution (CC BY) license (<https://creativecommons.org/licenses/by/4.0/>).

1. Introduction

Systems that transform electrical energy into mechanical energy are the basis of modern technology. Electric drives of different types consume about 50% of electric energy production (according to an official website of the European Union Electric motors and variable speed drives (europa.eu)) [1]. Precise and energy-efficient control of motion plays a fundamental role in all fields of technology, and their effective operation determines the completion of important tasks in production, transport, mining, medicine, bioengineering, etc. A standard assumption underlying typical models of motion transmission systems is that all components consist only of rigid bodies and ideal couplings. Under this assumption, the position and velocity of the load are the same as the position and velocity of the motoring shaft. Unfortunately, this is an idealized situation that may be considered valid only in the case of slow motion and small interacting forces/torques. In general, mechanical flexibility is present in most motion transmission systems. This introduces static and dynamic deflections between the position of the driving actuators and the position of the manipulated part. Such a drive system can be modeled as a so-called two-mass system. The motoring part (the first mass) is connected by a flexible joint with the manipulated part (the second mass). Numerous applications are based on the two-mass model, and some of them are rolling mill drives [2], conveyer belt drives [3], cage-hoist drives [4,5], drilling rigs used in oil and gas explorations [6,7], some special drives used in textile [8] and paper machines [9,10], space antennas [11,12] and space manipulators [13,14], CNC drives [15], wind turbines [16], microelectromechanical systems (MEMS) [17], robotic manipulators with flexible joints [18], electric drives using harmonic reducers [19] and planetary gear powertrains [20,21]. Among the above-mentioned applications, manipulators with flexible joints are of particular interest. First, the two-mass model well reflects the behavior of a single manipulator segment. Second, potential implementations are

wide and include not only industrial robots but also medical, rehabilitation, space and human-cooperating manipulators.

The mechanical flexibility of robotic manipulators is introduced by two main factors: the use of compliant transmission elements and the flexibility of links. In some applications (for instance, space manipulators), a reduction in the mass of the links is so important that the flexibility of the link caused by a slender construction or the application of lightweight materials is accepted. Normally, the flexibility of industrial manipulators results from the use of flexible joints. Numerous examples of robots with flexible joints are reported in [22]. Mechanical flexibility is common, when motion reduction is performed by belts, long shafts, cables, harmonic drives and cycloidal gears. Recently, flexible transmission elements have also been deliberately included in the construction of direct-drive robotic joints using fast, permanent magnet motors. Some of them are used to reduce rotation axis misalignment, improving reliability and extending the lifetime, whereas others are aimed at improving the safety of robot–human cooperation and modifying the movement of the robot arm. There are multiple constructions of such elements, and different materials are used. For instance, Figure 1a presents a simple coupling with a polymer insert. Refs. [23,24] describe the construction of a Variable Stiffness Actuator (VSA), and ref. [25] presents a concept of serial elastic actuation that utilizes one or more series elastic elements to intentionally improve the dynamic and control properties of the system.

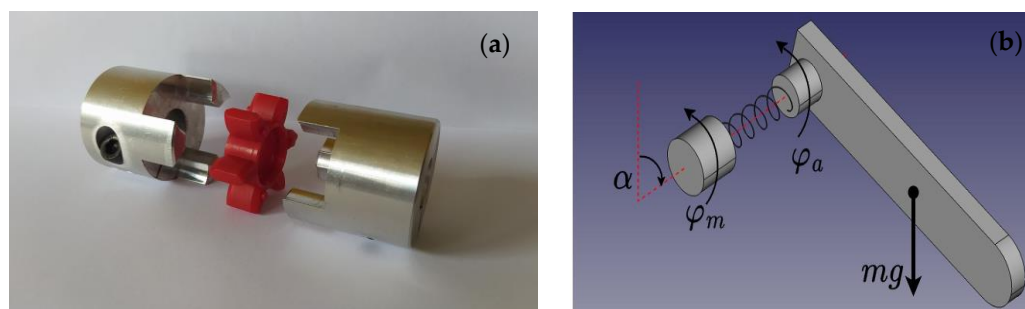


Figure 1. Exemplary coupling with a nonlinear stiffness (a) and schematic representation of an elastic joint (b): φ_a —angular position of the arm, φ_m —motor shaft position, mg —gravity, α —angle between the motor axis and the vertical.

For all these constructions (and numerous others modeled as a two-mass system), it is common that the torque transmitted by a flexible joint cannot be modeled as proportional to the torsion angle. It is rather represented by a ‘stiffness curve’, which is a significantly nonlinear although monotonically increasing convex or concave curve. This observation is also confirmed by the experiments reported in this paper.

Other phenomena that strongly affect position control are any torques affecting both sides of the joint. Their main source is friction, and in this case, they oppose movement. However, they can also come from gravitational forces and other interactions related to the specific task performed by the two-mass system. These highly nonlinear torques, together with the flexibility of the joint, are the reason for the most important problem: torsional oscillations that impair the precision of position control and may cause breakdowns and damages.

Therefore, the main challenge for the position controller for a two-mass system presented here is to assure sufficiently precise position tracking, despite the following:

- Unknown or changing parameters of the motor, the load and the joint;
- Unknown nonlinear torques acting on both sides of the flexible joint;
- An unknown nonlinear “stiffness curve” describing the transmitted torque as a function of the torsion angle.

We consider a two-mass model to demonstrate the derivation and the features of the obtained controller, but the proposed derivation can be generalized to a multi-degree-of-freedom case. Finally, an appropriate real plant (an arm moved by a flexible shaft

connecting it with a permanent magnet synchronous motor) is used to demonstrate the practical applicability of the proposed approach.

Almost all existing solutions for the position control of a two-mass drive with a flexible shaft assume that the stiffness coefficient is constant and the transmitted torque is proportional to the torsion angle. Early works come from the 20th century and are mostly based on linear control theory: PD control, PD with gravity compensation and full-state feedback. The development of the nonlinear control theory resulted in the application of its achievements. The feedback linearization approach and passivity-based approach were the first to be applied to position control but were based on the exact model of the plant. An extensive bibliography of the subject is discussed in [22]. Some more recent approaches to the design of controllers for two-mass systems include the linear quadratic regulator (LQR), root locus, etc. [26]; artificial intelligence-based methods—artificial neural networks [27], linear model predictive control [28] and fuzzy controllers [29]; and nonlinear control techniques—nonlinear neural networks [30,31], adaptive nonlinear control [32–34] and the wave-based disturbance observer approach [35]. The control of a robotic arm with a flexible joint is still a challenging topic, and new publications keep popping up. Among very recent papers, in [36], a kind of external linearization is used that requires an arm-mounted accelerometer. Ref. [37] considers the impact of measurement errors on the nonlinear control of a flexible-joint robot. Ref. [38] is among a few studying nonlinear friction. In [39], position tracking in a two-mass system is solved with a concept founded on a robust observer design based on a linear matrix inequality (LMI) solution. The observer cooperates with the original nonlinear controller.

None of these papers take into account the nonlinear nature of stiffness. A recent paper [40] refers to nonlinear stiffness but is devoted to the development of a desired velocity-tracking controller. Therefore, here, we present a novel controller that

- Solves a position tracking problem for a two-mass drive with a flexible joint;
- Takes into account a nonlinear ‘stiffness curve’ of the joint and takes advantage by using it for control purposes;
- Operates correctly in the presence of unknown nonlinear torques acting on both sides of the joint;
- Operates correctly even if all plant parameters are unknown.

The derivation of the controller is based on nonlinear adaptive control theory, and a proof of the uniform ultimate boundedness of tracking errors is presented. The simplicity of the obtained controller was an important aim of the proposed approach. It was obtained by eliminating some loops in a backstepping-like design. The dynamic surface approach (command control filtering) was used to calculate the derivatives of virtual controls with linear filters, instead of analytically. This prevents ‘the explosion of complexity’ in the resulting expressions describing the controller. The second-order filters proposed here enable smoother control. Thanks to a well-thought-out derivation, we obtained a control algorithm that can be implemented in a DSP processor.

The derived controller was implemented with a DSP in a real control plant. The constructed laboratory stand imitates a joint with nonlinear stiffness characteristics. The impact of important factors omitted during the design, such as the sampling time, unmodeled dynamics, quantization, etc., was investigated and discussed. It was demonstrated that the implemented controller is able to operate correctly even if the characteristic of the joint is changed. All conducted experiments are an important part of the presented novel result, prove the value of the derived control algorithm and testify to the possibilities of its practical use.

Finally, we compare the proposed approach with one of the recent solutions presented in [41,42] and demonstrate that we are able to obtain smaller tracking errors.

2. Plant Model and Problem Statement

Modeling a two-mass system can be achieved using several approaches. If the shaft is long, axial, torsional and lateral vibrations occur, and distributed parameter models are

recommended [43,44]. If delays connected with the oscillatory waves traveling through the shaft are significant, neutral-type time-delay models [45,46] can be applied. But in numerous applications such as robotic manipulators (and many others), when the flexible joint is very compact, lumped parameter models obtained from Euler–Lagrange equations are fully adequate.

Direct-drive permanent magnet motors commonly used in advanced two-mass drives are very fast. Therefore, it is possible to assume that the torque/current control loop operates approximately as a proportional element and that the desired current is an actual control input of the plant. Of course, robustness against the unmodeled current control loop dynamics should be investigated.

The assumption that both the motor and arm positions are measured is a little restrictive, but it is possible in numerous applications. For instance, more and more commercially available complete robotic joints offer this opportunity (see TECHSOFT ROBOTS, Sierramotion, Celera, etc.).

Friction is modeled as a nonlinear algebraic function of velocity, for instance, the Stribeck curve, which is commonly acceptable [38].

The damping of the joint is assumed to be negligible. Finally, nonlinear stiffness is modeled, according to the literature and our own experiments, as a nonlinear monotonically increasing convex or concave curve with unknown parameters.

All these remarks justify the selected model of the two-mass drive presented below.

A load (for instance, a robotic arm) is modeled as a rigid body, according to Newton's dynamic principle:

$$J_a \dot{\omega}_a = S(\varphi) - T_a T_{fa}(\omega_a) - c_a \omega_a - bM(\varphi_a), \quad (1)$$

where φ_a denotes the angular position of the load, ω_a denotes the angular velocity and J_a is the unknown inertia of the load. The remaining components in Equation (1) represent the torques influencing the load. Thus, T_a , $T_{fa}(\omega_a)$, $c_a \omega_a$ represent the friction affecting the motion of the load. Parameters T_a , c_a , are unknown. Function $T_{fa}(\omega_a)$ is used to model the nonlinear part of friction, for instance, to introduce the Stribeck curve effect. Component $bM(\varphi_a)$, where the coefficient b is unknown, characterizes the torque caused by any external forces, like gravitation, etc. For instance, if the load is an arm situated as in Figure 1b and works against gravity, we have $M(\varphi_a) = \sin \alpha \sin \varphi_a$. Of course, it is possible to use more than one unknown parameter to parameterize each of the torques affecting the motion, but one parameter for each component representing the torque of a different physical nature is enough because, finally, all components form a scalar function in Equation (1).

The propelling torque in Equation (1), transmitted by a flexible joint, is represented by $S(\varphi)$, where φ stands for the torsion angle caused by a flexible joint or shaft; it is the angular displacement between the motor shaft position φ_m and the load position.

$$\varphi = \varphi_m - \varphi_a. \quad (2)$$

This torque is modeled as a linear combination of a linear and nonlinear component:

$$S(\varphi) = p_1 \varphi + p_2 S_n(\varphi) \quad (3)$$

with unknown coefficients $p_1 > 0$, p_2 , where the derivative $\frac{dS_n(\varphi)}{d\varphi}$ is bounded. It is assumed that the damping in the flexible joint is negligible, so no torque proportional to $\dot{\varphi}$ appears in Equation (1).

Finally, the motoring part of the drive is described by

$$J_m \dot{\omega}_m = -S(\varphi) - T_m T_{fm}(\omega_m) - c_m \omega_m + k_i i_r, \quad (4)$$

where ω_m is the motor angular velocity, J_m is the motor inertia, $T_m T_{fm}(\omega_m) + c_m \omega_m$ represents the motor friction analogously as in Equation (1) and $k_i i_r$ is the propelling torque, proportional to the reference motor current i_r . This assumption is valid for permanent magnet synchronous motors (PMSMs) with surface-mounted permanent magnets (where q- and d-axis inductances are equal) or for interior permanent magnet construction if the d-axis current reference is zero. Parameters J_m, T_m, c_m and k_i are unknown. The proposed model is a nonlinear two-mass system with unknown parameters. It includes a nonlinear stiffness characteristic and nonlinear friction acting on both sides of a flexible joint. All parameters are unknown, but of course, some estimations that can be used as the starting values of adaptive parameters could be useful. The reference current i_r is the input signal to the current control loop, including a fast PI controller, so we can assume that the actual current i equals the desired value $i_r \approx i$ and that the electromagnetic torque is proportional to the desired current.

The control's aim is to follow a desired smooth position trajectory $\varphi_d(t)$ with the actual load position $\varphi_a(t)$, despite the unknown parameters.

3. Adaptive Controller

Let us define the tracking error as

$$e = \varphi_d - \varphi_a \tag{5}$$

and the augmented tracking error as

$$e_a = e + \tau_0 \dot{e} = \varphi_d - \varphi_a + \tau_0 (\dot{\varphi}_d - \omega_a). \tag{6}$$

The tracking error e is the response of the inertial filter with the transfer function $\frac{1}{s\tau_0+1}$ to the input e_a , so the filter time constant $\tau_0 > 0$ is the first design parameter. The controller is derived in a recursive way, leading to successive control loops.

Loop 1

It follows directly from Equations (1) and (6) that

$$\dot{e}_a = \dot{\varphi}_d - \omega_a + \tau_0 \ddot{\varphi}_d - \frac{\tau_0}{J_a} (p_1 \varphi + p_2 S_n(\varphi) - T_a T_{fa}(\omega_a) - c_a \omega_a - bM(\varphi_a)). \tag{7}$$

After introducing notation $p_{21} := \frac{p_2}{p_1}$ and assuming that the unknown parameter p_{21} is substituted by the adaptive parameter \hat{p}_{21} , where $\tilde{p}_{21} := p_{21} - \hat{p}_{21}$ represents the adaptation error, Equation (7) is transformed into

$$\frac{J_a}{\tau_0 p_1} \dot{e}_a = \frac{J_a}{p_1} \frac{1}{\tau_0} (\dot{\varphi}_d - \omega_a + \tau_0 \ddot{\varphi}_d) - \varphi - \frac{p_2}{p_1} S_n(\varphi) + \frac{T_a}{p_1} T_{fa}(\omega_a) + \frac{c_a}{p_1} \omega_a + \frac{b}{p_1} M(\varphi_a) \tag{8}$$

and finally into the abbreviated form

$$\frac{J_a}{\tau_0 p_1} \dot{e}_a = \theta_a^T \xi_a - \varphi - \hat{p}_{21} S_n(\varphi) - \tilde{p}_{21} S_n(\varphi), \tag{9}$$

where

$$\theta_a^T = \left[\frac{J_a}{p_1} \quad \frac{T_a}{p_1} \quad \frac{c_a}{p_1} \quad \frac{b}{p_1} \right] \tag{10}$$

is the vector of the unknown parameters and

$$\xi_a^T = \left[\frac{1}{\tau_0} (\dot{\varphi}_d - \omega_a + \tau_0 \ddot{\varphi}_d) \quad T_{fa}(\omega_a) \quad \omega_a \quad M(\varphi_a) \right] \tag{11}$$

is formed by known functions. The unknown parameters θ_a are substituted by the adaptive parameters $\hat{\theta}_a$, and the error of adaptation is denoted by $\tilde{\theta}_a = \theta_a - \hat{\theta}_a$. The signal

$\psi := \varphi + \hat{p}_{21}S_n(\varphi)$ (a virtual control in Equation (9)), is shaped to follow the desired trajectory ψ_d (a stabilizing function) to stabilize Equation (9). The gap between ψ_d and ψ is denoted by

$$e_\psi = \psi_d - \psi. \tag{12}$$

Therefore, Equation (9) is considered in the form

$$\frac{J_a}{\tau_0 p_1} \dot{e}_a = \theta_a^T \zeta_a - \psi_d + e_\psi - \tilde{p}_{21} S_n(\varphi). \tag{13}$$

The stabilizing function is selected as

$$\psi_d = \hat{\theta}_a^T \zeta_a + k_a e_a + \frac{1}{2} e_a, \tag{14}$$

where $k_a > 0$ is the design parameter responsible for the final dynamics of the signal e_a . Component $\hat{\theta}_a^T \zeta_a$ in (14) is supposed to cancel $\theta_a^T \zeta_a$ in (13), and $k_a e_a + \frac{1}{2} e_a$ is used to stabilize e_a . After plugging in the stabilizing Function (14) into Equation (13), we obtain

$$\frac{J_a}{\tau_0 p_1} \dot{e}_a = -k_a e_a + \tilde{\theta}_a^T \zeta_a + e_\psi - \tilde{p}_{21} S_n(\varphi) - \frac{1}{2} e_a. \tag{15}$$

Next, the dynamics of the error e_ψ must be considered. Instead of deriving an analytical form of $\dot{\psi}_d$ (necessary to find \dot{e}_ψ), to avoid an ‘explosion of complexity’, we introduce a second-order linear filter, the first of two we plan to use, described by

$$\begin{aligned} \dot{z}_{11} &= z_{12}, \\ \dot{z}_{12} &= \frac{1}{a_{12}} (\psi_d - z_{11} - a_{11} z_{12}). \end{aligned} \tag{16}$$

To make the design clearer, parameters a_{11} , a_{12} are selected so that the filter characteristic polynomial $a_{12}s^2 + a_{11}s + 1$ possesses a double real negative pole $\frac{-1}{\tau_1}$. In this case, $\tau_1 > 0$ represents the filter time constant, and the characteristic polynomial becomes $M(s) = (\tau_1 s + 1)^2 = \tau_1^2 s^2 + 2\tau_1 s + 1$. In Equation (16), we have $a_{12} = \tau_1^2$, $a_{11} = 2\tau_1$, $\frac{a_{11}}{a_{12}} = \frac{2}{\tau_1}$. As the transient of the filter vanishes, z_{11} tends to ψ_d , so z_{12} tends to $\dot{\psi}_d$. We introduce the following new variables:

$$\begin{aligned} \rho_\psi &= \psi_d - z_{11} \\ \rho_{\psi 1} &= \dot{\rho}_\psi = \dot{\psi}_d - z_{12}. \end{aligned} \tag{17}$$

The dynamic of the variables in (17) can be described by

$$\begin{aligned} \dot{\rho}_\psi &= \rho_{\psi 1} \\ \dot{\rho}_{\psi 1} &= -\frac{1}{\tau_1} \rho_\psi - \frac{2}{\tau_1} \rho_{\psi 1} + \ddot{\psi}_d + \frac{2}{\tau_1} \dot{\psi}_d. \end{aligned} \tag{18}$$

Equation (18) can be rewritten in the following form:

$$\dot{\rho}_1 = A_{\rho 1} \rho_1 + B_{\rho 1} \left(\ddot{\psi}_d + \frac{2}{\tau_1} \dot{\psi}_d \right) = A_{\rho 1} \rho_1 + B_{\rho 1} H_1(*) \tag{19}$$

where

$$A_{\rho 1} = \begin{bmatrix} 0 & 1 \\ -\frac{1}{\tau_1^2} & -\frac{2}{\tau_1} \end{bmatrix}, B_{\rho 1} = \begin{bmatrix} 0 \\ 1 \end{bmatrix}, \rho_1 = \begin{bmatrix} \rho_\psi \\ \rho_{\psi 1} \end{bmatrix}$$

and $H_1 = \ddot{\psi}_d + \frac{2}{\tau_1} \dot{\psi}_d$.

After multiplying both sides by τ_1 , we have

$$\tau_1 \dot{\rho}_1 = A_{\rho 1} \tau_1 \rho_1 + B_{\rho 1} (\tau_1 \ddot{\psi}_d + 2\dot{\psi}_d) = A_{\rho 1} \tau_1 \rho_1 + B_{\rho 1} H_{1\tau} (*) \quad (20)$$

and $H_{1\tau} = \tau_1 \ddot{\psi}_d + 2\dot{\psi}_d$ is a continuous function of variables $\varphi_d, \dot{\varphi}_d, \ddot{\varphi}_d, \varphi_d^{(3)}, \varphi_d^{(4)}, e_a, \rho_1$, as well as of some other variables, $e_{\psi f}, e_{\omega f}$ and $\tilde{\theta}_a, \tilde{p}_{21}, \rho_2$, which are defined during the derivation of the controller. On any compact set, the function $H_{1\tau}$ is bounded. In addition, since $|H_{1\tau}|$ decreases with decreasing τ_1 , for sufficiently small τ_1 ($\tau_1 < \tau_{1suf}$), we have $|H_{1\tau} (*)| \leq M_1$, and M_1 does not depend on the filter parameter τ_1 .

Instead of investigating the error e_ψ , we define the filtered error as

$$e_{\psi f} = z_{11} - \psi \quad (21)$$

which, because of (12) and (17), differs from e_ψ by component ρ_ψ :

$$e_{\psi f} = z_{11} - \psi = z_{11} + e_\psi - \psi_d = e_\psi - \rho_\psi \Leftrightarrow e_\psi = e_{\psi f} + \rho_\psi. \quad (22)$$

The substitution of (22) into (15) provides

$$\frac{J_a}{\tau_0 p_1} \dot{e}_a = -k_a e_a + \tilde{\theta}_a^T \zeta_a + e_{\psi f} + \rho_\psi - \tilde{p}_{21} S_n(\varphi) - \frac{1}{2} e_a. \quad (23)$$

Loop 2

Next, using Equations (1), (2), (4) and (22), the behavior of $e_{\psi f}$ can be described by

$$\begin{aligned} \dot{e}_{\psi f} &= \dot{z}_{11} - \dot{\psi} = z_{12} - \frac{d}{dt}(\varphi + \hat{p}_{21} S_n(\varphi)) \\ &= z_{12} - \omega_m + \omega_a - \dot{\hat{p}}_{21} S_n(\varphi) - \hat{p}_{21} \frac{dS_n(\varphi)}{d\varphi} (\omega_m - \omega_a) \\ &= z_{12} - \left(1 + \hat{p}_{21} \frac{dS_n(\varphi)}{d\varphi}\right) \omega_m + \left(1 + \hat{p}_{21} \frac{dS_n(\varphi)}{d\varphi}\right) \omega_a - \dot{\hat{p}}_{21} S_n(\varphi). \end{aligned} \quad (24)$$

We try to shape ω_m (virtual control) to stabilize $e_{\psi f}$. The desired trajectory for ω_m is denoted by ω_{md} , and the tracking error is denoted by $e_\omega = \omega_{md} - \omega_m$. Therefore,

$$\dot{e}_{\psi f} = z_{12} - \left(1 + \hat{p}_{21} \frac{dS_n(\varphi)}{d\varphi}\right) (\omega_{md} - e_\omega) + \left(1 + \hat{p}_{21} \frac{dS_n(\varphi)}{d\varphi}\right) \omega_a - \dot{\hat{p}}_{21} S_n(\varphi). \quad (25)$$

The stabilizing function ω_{md} is supposed to stabilize the system described by Equations (23) and (25); hence, it is selected as

$$\omega_{md} = \omega_a + \frac{1}{1 + \hat{p}_{21} \frac{dS_n(\varphi)}{d\varphi}} \left(z_{12} - \dot{\hat{p}}_{21} S_n(\varphi) + k_\psi e_{\psi f} + e_a \right) + \frac{1}{2} \left(1 + \hat{p}_{21} \frac{dS_n(\varphi)}{d\varphi} \right) e_{\psi f} \quad (26)$$

where $k_\psi > 0$ is the next design parameter responsible for the dynamics of $e_{\psi f}$. The subsequent components in (26) are supposed to cancel unnecessary components in (25) or stabilize systems (23) and (25), as becomes clear during the final Lyapunov function investigation. The factor $1 + \hat{p}_{21} \frac{dS_n(\varphi)}{d\varphi}$ should be kept as far from zero as possible to avoid singularity and high values of ω_{md} , and this is assured by the proper adaptation of parameter \hat{p}_{21} . Under the stabilizing function ω_{md} defined in (26), the dynamics of $e_{\psi f}$ given by Equation (25) are reduced to

$$\dot{e}_{\psi f} = -k_\psi e_{\psi f} - e_a + \left(1 + \hat{p}_{21} \frac{dS_n(\varphi)}{d\varphi}\right) e_\omega - \frac{1}{2} \left(1 + \hat{p}_{21} \frac{dS_n(\varphi)}{d\varphi}\right)^2 e_{\psi f}, \quad (27)$$

so both components, $-k_\psi e_{\psi f}$ and $-\frac{1}{2} \left(1 + \hat{p}_{21} \frac{dS_n(\varphi)}{d\varphi}\right)^2 e_{\psi f}$, work for the stabilization of $e_{\psi f}$.

At the final stage of the design procedure, an investigation of e_ω is necessary, requiring the derivative of ω_{md} . Again, analogous to the previous stage, to avoid an ‘explosion of complexity’, the derivative is calculated with another filter defined by

$$\begin{aligned} \dot{z}_{21} &= z_{22}, \\ \dot{z}_{22} &= \frac{1}{a_{22}}(\omega_{md} - z_{21} - a_{21}z_{22}). \end{aligned} \quad (28)$$

Parameters a_{21} , a_{22} are selected so that the filter characteristic polynomial $a_{22}s^2 + a_{21}s + 1$ possesses a double real negative pole $-\frac{1}{\tau_2}$. In this case, $\tau_2 > 0$ represents the filter time constant, and the characteristic polynomial becomes $M(s) = (\tau_2 s + 1)^2 = \tau_2^2 s^2 + 2\tau_2 s + 1$, $\tau_2 > 0$. In Equation (28), we have $a_{22} = \tau_2^2$, $a_{21} = 2\tau_2$, $\frac{a_{21}}{a_{22}} = \frac{2}{\tau_2}$. As the transient of the filter vanishes, z_{21} tends to ω_{md} , so z_{22} tends to $\dot{\omega}_{md}$. We introduce the following new variables:

$$\begin{aligned} \rho_\omega &= \omega_{md} - z_{21} \\ \rho_{\omega 1} &= \dot{\omega}_{md} - z_{22} \end{aligned} \quad (29)$$

The dynamic of the variables in (29) can be described by

$$\begin{aligned} \dot{\rho}_\omega &= \rho_{\omega 1} \\ \dot{\rho}_{\omega 1} &= -\frac{1}{\tau_2}\rho_\omega - \frac{2}{\tau_2}\rho_{\omega 1} + \ddot{\omega}_{md} + \frac{2}{\tau_2}\dot{\omega}_{md} \end{aligned} \quad (30)$$

Equation (30) can be rewritten in the following form:

$$\dot{\rho} = A_{\rho 2}\rho_2 + B_{\rho 2}\left(\ddot{\omega}_{md} + \frac{2}{\tau_2}\dot{\omega}_{md}\right) = A_{\rho 2}\rho_2 + B_{\rho 2}H_2(*) \quad (31)$$

where $A_{\rho 2} = \begin{bmatrix} 0 & 1 \\ -\frac{1}{\tau_2^2} & -\frac{2}{\tau_2} \end{bmatrix}$, $B_{\rho 2} = \begin{bmatrix} 0 \\ 1 \end{bmatrix}$, $\rho_2 = \begin{bmatrix} \rho_\omega \\ \rho_{\omega 1} \end{bmatrix}$ and $H_2 = \ddot{\omega}_{md} + \frac{2}{\tau_2}\dot{\omega}_{md}$.

After multiplying both sides of (31) by τ_2 , we have

$$\tau_2 \dot{\rho}_2 = A_{\rho 2}\tau_2 \rho_2 + B_{\rho 2}(\tau_2 \ddot{\omega}_{md} + 2\dot{\omega}_{md}) = A_{\rho 2}\tau_2 \rho_2 + B_{\rho 2}H_{2\tau}(*) \quad (32)$$

and $H_{2\tau} = \tau_2 \ddot{\omega}_{md} + 2\dot{\omega}_{md}$ is a continuous function of variables $\varphi_d, \dot{\varphi}_d, \ddot{\varphi}_d, \varphi_d^{(3)}, \varphi_d^{(4)}, e_a, e_{\psi f}, e_{\omega f}, \tilde{\theta}_a, \tilde{p}_{21}, \tilde{\theta}_m, \rho_1, \rho_2$. On any compact set, the function $H_{2\tau}$ is bounded. In addition, since $|H_{2\tau}|$ decreases with decreasing τ_2 , for sufficiently small τ_2 ($\tau_2 < \tau_{2suf}$), we have $|H_{2\tau}(*)| \leq M_2$, and M_2 does not depend on the filter parameter τ_2 .

Instead of investigating the error e_ω , we define the filtered error as

$$e_{\omega f} = z_{21} - \omega_m \quad (33)$$

which differs from e_ω by a constrained component:

$$e_{\omega f} = z_{21} - \omega_m = z_{21} + e_\omega - \omega_{md} = e_\omega - \rho_\omega \Leftrightarrow e_\omega = e_{\omega f} + \rho_\omega. \quad (34)$$

The substitution of (34) into (27) provides

$$\dot{e}_{\psi f} = -k_\psi e_{\psi f} - e_a + \left(1 + \hat{p}_{21} \frac{dS_n(\varphi)}{d\varphi}\right)(e_{\omega f} + \rho_\omega) - \frac{1}{2} \left(1 + \hat{p}_{21} \frac{dS_n(\varphi)}{d\varphi}\right)^2 e_{\psi f}. \quad (35)$$

Loop 3

The transient of $e_{\omega f}$, which evidently affects $e_{\psi f}$, is described by the following derivation using Equation (4):

$$\frac{J_m}{k_i} \dot{e}_{\omega f} = \frac{J_m}{k_i} \dot{z}_{21} - \frac{J_m}{k_i} \dot{\omega}_m = \frac{J_m}{k_i} z_{22} + \frac{p_1}{k_i} \varphi + \frac{p_2}{k_i} S_n(\varphi) + \frac{T_m}{k_i} T_{fm}(\omega_m) + \frac{c_m}{k_i} \omega_m - i_r \quad (36)$$

and can be abbreviated to

$$\frac{J_m}{k_i} \dot{e}_{\omega f} = \theta_m^T \tilde{\xi}_m - i_r, \tag{37}$$

where

$$\theta_m^T = \left[\frac{J_m}{k_i} \quad \frac{T_m}{k_i} \quad \frac{c_m}{k_i} \quad \frac{p_1}{k_i} \quad \frac{p_2}{k_i} \right], \quad \tilde{\xi}_m^T = [z_{22} \quad T_{fm}(\omega_m) \quad \omega_m \quad \varphi \quad S_n(\varphi)]. \tag{38}$$

The vector of unknown parameters θ_m is substituted by adaptive parameters $\hat{\theta}_m$, and the error of adaptation is denoted by

$$\tilde{\theta}_m = \theta_m - \hat{\theta}_m. \tag{39}$$

The motor current, generating the propelling torque, must stabilize the complete system described by Equations (23), (35) and (37). Therefore, the control signal i_r is selected as

$$i_r = \hat{\theta}_m^T \tilde{\xi}_m + k_{\omega} e_{\omega f} + \left(1 + \hat{p}_{21} \frac{dS_n(\varphi)}{d\varphi} \right) e_{\psi f}, \tag{40}$$

where $k_{\omega} > 0$ is a design parameter, and using Equation (40), (31) transforms into

$$\frac{J_m}{k_i} \dot{e}_{\omega f} = -k_{\omega} e_{\omega f} + \tilde{\theta}_m^T \tilde{\xi}_m - \left(1 + \hat{p}_{21} \frac{dS_n(\varphi)}{d\varphi} \right) e_{\psi f}. \tag{41}$$

We introduce the notation $\rho_{\tau 1} = \tau_1 \rho_1$, $\rho_{\tau 2} = \tau_2 \rho_2$. The closed-loop system is described by differential Equations (20), (23), (32), (35) and (41). We must also design adaptive laws describing the behavior of adaptive parameters $\hat{\theta}_a, \hat{\theta}_m$ and \hat{p}_{21} , as well as the dynamics of adaptation errors $\tilde{\theta}_a, \tilde{\theta}_m, \tilde{p}_{21}$. The state variables of the closed-loop system are $e_a, e_{\psi f}, e_{\omega f}, \tilde{\theta}_a, \tilde{\theta}_m, \tilde{p}_{21}, \rho_{\tau 1}, \rho_{\tau 2}$. Therefore, final conclusions regarding the stability of the closed-loop system are derived from the analysis of the Lyapunov function, which, taking into account the right sides of Equations (23) and (41), is selected as

$$V \left(e_a, e_{\psi f}, e_{\omega f}, \tilde{\theta}_a, \tilde{\theta}_m, \tilde{p}_{21}, \rho_{\tau 1}, \rho_{\tau 2} \right) = \frac{1}{2} \left(\frac{J_a}{\tau_0 p_1} e_a^2 + e_{\psi f}^2 + \frac{J_m}{k_i} e_{\omega f}^2 \right) + \frac{1}{2} \left(\tilde{\theta}_a^T \Gamma_a^{-1} \tilde{\theta}_a + \frac{1}{\gamma_p} \tilde{p}_{21}^2 + \tilde{\theta}_m^T \Gamma_m^{-1} \tilde{\theta}_m \right) + \rho_{\tau 1}^T Q_1 \rho_{\tau 1} + \rho_{\tau 2}^T Q_2 \rho_{\tau 2}. \tag{42}$$

The Lyapunov function is parameterized by $\gamma_p > 0$ and positive definite matrices Γ_a, Γ_m and Q_1, Q_2 . Parameters $\gamma_p, \Gamma_a, \Gamma_m$ are design parameters and are used to tune adaptive laws, but matrices Q_1, Q_2 are not used in the controller equations and can be defined arbitrarily. This is shown in Appendix A, proving the main theorem. Parameters $\frac{J_a}{\tau_0 p_1}$ and $\frac{J_m}{k_i}$, which appear in the Lyapunov Function (42) (corresponding with the form of Equations (23) and (41)), are unknown but positive, and this is sufficient to prove the stability, as shown in Appendix A.

Finally, the selection of adaptive laws describing the behavior of the adaptive parameters completes the derivation of the controller. We use robust adaptive control laws for $\hat{\theta}_m$ and $\hat{\theta}_a$:

$$\dot{\hat{\theta}}_m = \Gamma_m \left(\tilde{\xi}_m e_{\omega f} - \sigma_m \hat{\theta}_m \right), \quad \dot{\hat{\theta}}_a = \Gamma_a \left(\tilde{\xi}_a e_a - \sigma_a \hat{\theta}_a \right) \tag{43}$$

with small positive ‘leakage parameters’ σ_m, σ_a .

Special care is required for the adaptation of \hat{p}_{21} because it appears in the denominator of the stabilizing Function (26). Therefore, we use a projection operator:

$$\dot{\hat{p}}_{21} = \gamma_p \text{Proj}_{p^m, p^M}(\gamma, \hat{p}_{21}) = \begin{cases} 0 & \text{if } \hat{p}_{21} \leq p^m \text{ and } \gamma < 0 \\ 0 & \text{if } \hat{p}_{21} \geq p^M \text{ and } \gamma > 0, \\ -\gamma_p \gamma & \text{otherwise} \end{cases} \tag{44}$$

$$\gamma = -S_n(\varphi) e_a - \sigma_P \hat{p}_{21}$$

with parameters p^m , p^M and $\sigma_p > 0$. This adaptive law guarantees that $p^m \leq \hat{p}_{21} \leq p^M$ and that

$$\tilde{p}_{21} \left(\gamma - \text{Proj}_{p^m, p^M}(\gamma, \hat{p}_{21}) \right) \leq 0. \quad (45)$$

Parameters p^m, p^M must be selected carefully to assure that, for a certain $\varepsilon > 0$, $\left| 1 + \hat{p}_{21} \frac{dS_n(\varphi)}{d\varphi} \right| > \varepsilon > 0$.

The following theorem formulates conclusions regarding the stability of the closed system and authorizes the use of the derived adaptive control.

Theorem 1. *The controller defined by stabilizing functions (14) and (26), filters (18) and (30) and the control (40), together with adaptive laws (43) and (44), ensures that the load position φ_a tracks any sufficiently smooth desired trajectory and that the tracking error is SGUUB (semiglobally uniformly ultimately bounded [47]), despite the parameters of the model (1)–(4) being unknown. All closed-loop signals are bounded. The proper choice of design parameters allows narrowing the set of attraction for uniformly ultimately bounded trajectories.*

The proof of the theorem is given in Appendix A.

4. Experimental Verification

4.1. Laboratory Stand

The laboratory stand used to verify the proposed controller is presented in Figure 2a.

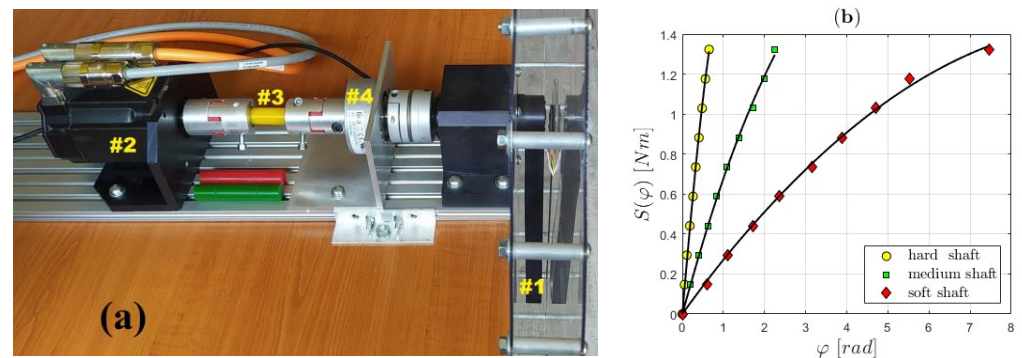


Figure 2. (a) Laboratory stand used to verify the proposed controller (explanations in the text) and (b) the identified joint stiffness characteristics.

The robotic arm (#1) is propelled by a permanent magnet synchronous motor AKM2G-41-P (#2) manufactured by Kollmorgen (Marengo, IA, USA). The flexible joint is completed by a polyurethane short shaft (#3) (length 45 mm, diameter 18 mm) and two elastic couplings. The arm position is measured by an encoder LIKA C80 (#4) (by Lika Electronic, Carrè, Italy). The motor position is measured by the built-in motor encoder. The resolution of both encoders is $2\pi/2^{13}$ rad. The motor is controlled by a PWM inverter controller AKD-T02406 (Kollmorgen, Radford, VA, USA) using only the current control loop, with the desired current i_r as the plant input. It is initially assumed that the current control loop works perfectly, so $i = i_r$. The feedback signals φ_a , φ_m are encoder outputs. The motor and arm angular velocities are calculated from the encoder data by inertial differentiating filters with time constants of 1 ms (for the motor) and 5 ms (for the arm). The complete adaptive algorithm is implemented with MicroLabBox DS1202 (dSPACE GmbH, Paderborn, Germany).

4.2. Plant Modeling

The model (1)–(4) of the plant was compared with the measurement results. The final model parameters were tuned after performing several step response experiments and curve fitting via genetic optimization. This was performed using the Simulink and

Optimization and Global Optimization toolboxes from Matlab ver. 2020a. But first, the structure of the model and the initial values of the parameters must be selected.

One can expect that the friction affecting the motor and the arm is quite a complicated nonlinear phenomenon, especially for small velocity values. Unfortunately, the identification of a complete Stribeck curve, which definitely comes out in real bearings, requires tedious experiments with precise velocity measurements. Therefore, for design purposes, the friction model is simplified to the form $c_m\omega_m + T_m \tanh(K_m\omega_m)$ for the motor and, analogously, $c_a\omega_a + T_a \tanh(K_a\omega_a)$ for the arm.

The current control loop is simplified to a proportional block $i = i_r$, and the torque constant in Equation (4) is known from the motor data: $k_i = 0.147 \text{ Nm/A}$. This can be a good initial guess for the unknown k_i . Although no adaptive parameter represents k_i explicitly, k_i appears in the set of parameters $\left[\frac{J_m}{k_i} \quad \frac{T_m}{k_i} \quad \frac{c_m}{k_i} \quad \frac{p_1}{k_i} \quad \frac{p_2}{k_i} \right]$, which are substituted by adaptive parameters $\hat{\theta}_m$.

Because of the position of the drive, the action of gravity is modeled by $bM(\varphi_a) = b\sin\varphi_a$. The transmitted torque model (3) is slightly modified to include the damping:

$$S(\varphi, \dot{\varphi}) = p_1\varphi + p_2S_n(\varphi) + \beta\dot{\varphi}. \quad (46)$$

The step responses of the drive were determined for the constant desired currents $i_r = 0, 1, 2, \dots, 9 \text{ A}$, corresponding to steady-state torques from 0 to 1.32 Nm. For each experiment, the steady state values of positions φ_a, φ_m were recorded, and the corresponding transmitted torque was calculated. The obtained data points are presented in Figure 2b. The linear mean square approximation of the obtained data by $S(\varphi, 0) = p_1\varphi + p_2S_n(\varphi) = p_1\varphi + p_2 \tanh(\varphi)\varphi^2$ provides $[p_1, p_2] = [0.731, -0.0704]$ for the medium shaft, $[p_1, p_2] = [2.3445, -0.8768]$ for the hard shaft and $[p_1, p_2] = [0.2815, -0.0136]$ for the soft shaft. The obtained stiffness characteristics $S(\varphi, 0)$ are plotted in Figure 2b. The stiffness curve was identified several times for a new shaft and after several periods of exploitation of the drive. The shape of the curve remained unchanged, and the identified parameters agreed with the limits of numerical precision. The external temperature may have had some influence on the stiffness curve parameters, but the adaptive control algorithm derived here was able to compensate for such changes.

The stiffness of the shaft has a decisive influence on the behavior of the drive, which is shown in Figure 3, presenting the angle of the shaft torsion during the step response for different couplings.

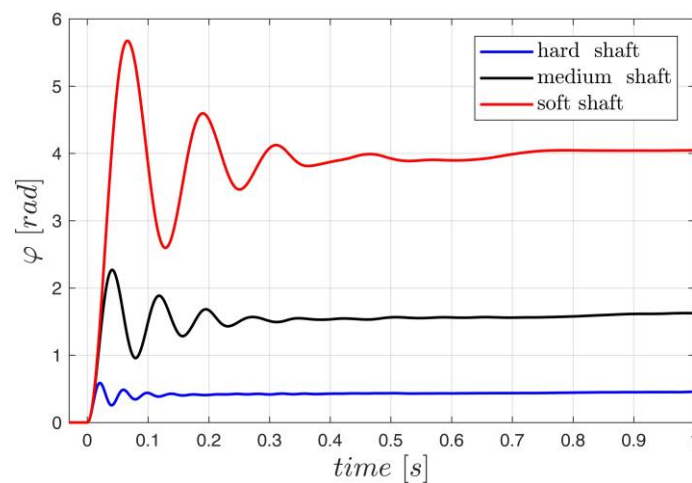


Figure 3. Step response of the model, $i_r = 7 \text{ A}$ —shaft torsion angle for different shafts.

The initial values of parameters $J_m, T_m, c_m, J_a, T_a, c_a$ and β were obtained from the motor data and geometry of the arm. The final values of parameters were calculated from the step responses of the open-loop drive via curve fitting with genetic optimization. The

initial and the final values of parameters are presented in Table 1. The medium flexible shaft was used during those experiments.

Table 1. Model parameters.

Parameter	Initial	Final
J_m	$7.74 \times 10^{-5} \text{ kgm}^2$	$7.6 \times 10^{-5} \text{ kgm}^2$
T_m	0.023 Nm	0.0106 Nm
c_m	$4.3 \times 10^{-5} \text{ Nms/rad}$	$9.5 \times 10^{-5} \text{ Nms/rad}$
J_a	0.0264 kgm ²	0.0271 kgm ²
T_a	0.019 Nm	0.0158 Nm
c_a	$7.1 \times 10^{-3} \text{ Nms/rad}$	$8.8 \times 10^{-3} \text{ Nms/rad}$
β	0	0.0022 Nms/rad
b	1.36 Nms/rad	1.347 Nms/rad

The obtained model of the drive was compared with the data obtained from the open-loop experimental system. In Figure 4, the measured position of the motor and the shaft is compared with those calculated by the model.

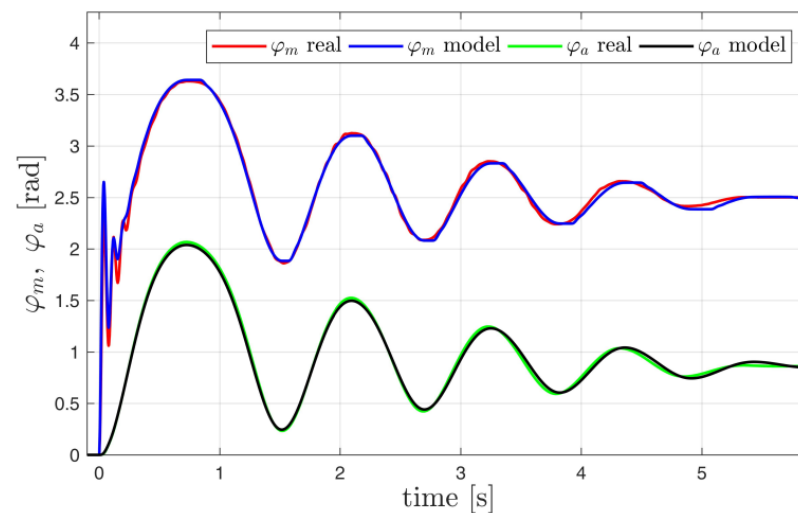


Figure 4. Step response of the model and the real plant, $i_r = 7A$ —motor and arm position for the model and the plant.

Figure 5 demonstrates the model and the plant response for a variable frequency signal $i_r(t) = 2\sin\left(2\pi\left(10^{\frac{3t}{100}} - 1\right)t\right)$; the frequency is changed logarithmically from 0.1 Hz to 100 Hz.

The presented experiments can be summarized by stating that the accuracy of the obtained model is sufficient but not perfect.

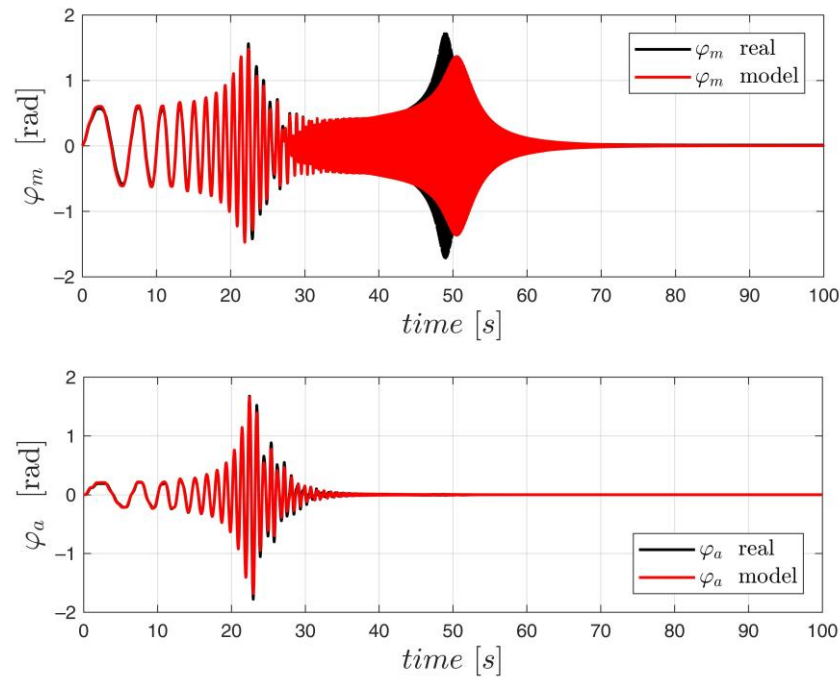


Figure 5. Response of the model and the real plant, $i_r(t) = 2\sin\left(2\pi\left(10^{\frac{3t}{100}} - 1\right)t\right)$.

4.3. Numerical Experiments

Before implementing the derived adaptive controller for the real drive, several simulation experiments were conducted to tune the parameters initially and to test the main features of the controller. The simulations were performed using Simulink ver. 10.1. This software allows the generation of code executable by an dSPACE DS1102 DSP board (dSPACE GmbH, Paderborn, Germany). The controller parameters are collected and described in Table 2.

Table 2. Controller design parameters.

Parameters	Responsibility	Values (in Proper SI Units)
τ_0	Augmented error filter time constant	$\tau_0 = 1$
k_a, k_ψ, k_ω	Error feedback gains, decreasing steady-state error, shortening the system transient, increasing control values	$k_a = k_\psi = k_\omega = 1$
$\tau_i, i = 1, 2$	Time constants of differentiating filters	$\tau_i = 10^{-4}, i = 1, 2$
$\gamma_p > 0$ and positive definite matrices Γ_a, Γ_m	Lyapunov function coefficients, increasing the speed of adaptation	$\gamma_p = 0.01$ $\Gamma_a = \text{diag}([0.03, 0.1, 0.03, 1])$ $\Gamma_m = \text{diag}([10^{-6}, 10^{-2}, 10^{-4}, 1, 0.1])$
$\sigma_a, \sigma_m, \sigma_p$	Small, positive ‘leakage’ parameters for adaptive laws; make adaptive laws more robust, and if too big, they can increase the quasi-steady-state error	$\sigma_a = \sigma_m = \sigma_p = 0.001$
p^m, p^M	Projection parameters for the adaptation of \hat{p}_{21} must be selected carefully to assure that $\left 1 + \hat{p}_{21} \frac{dS_n(\varphi)}{d\varphi}\right > \varepsilon > 0$	$p^m = 1.5 \frac{p_2}{p_1}, (p_2 < 0)$ $p^M = 1000;$
$\hat{\theta}_a(0), \hat{\theta}_m(0), \hat{p}_{12}(0)$	Initial conditions for adaptive parameters; should be selected to estimate $\begin{bmatrix} J_a & T_a & c_a & b \\ p_1 & p_1 & p_1 & p_1 \end{bmatrix} \begin{bmatrix} J_m & T_m & c_m & p_1 & p_2 \\ k_i & k_i & k_i & k_i & k_i \end{bmatrix}$ and $\frac{p_2}{p_1}$	Zero

During the first simulation, the plant was modeled by Equations (1)–(4) with the parameters obtained in Section 4.2. The arm was supposed to track the desired position trajectory $\varphi_d = 2\sin(t)$ [rad]. This demonstrates the typical operation of a robotic servo. The initial values of the adaptive parameters were selected as zero, thereby modeling the complete ignorance of the real parameters. The remaining controller parameters were taken from Table 2. As demonstrated in Figure 6, the system operates properly—all errors approach zero (actually, $\sim 3 \cdot 10^{-4}$ [rad] for $t > 1000$ s because of a rather large filter time constant).

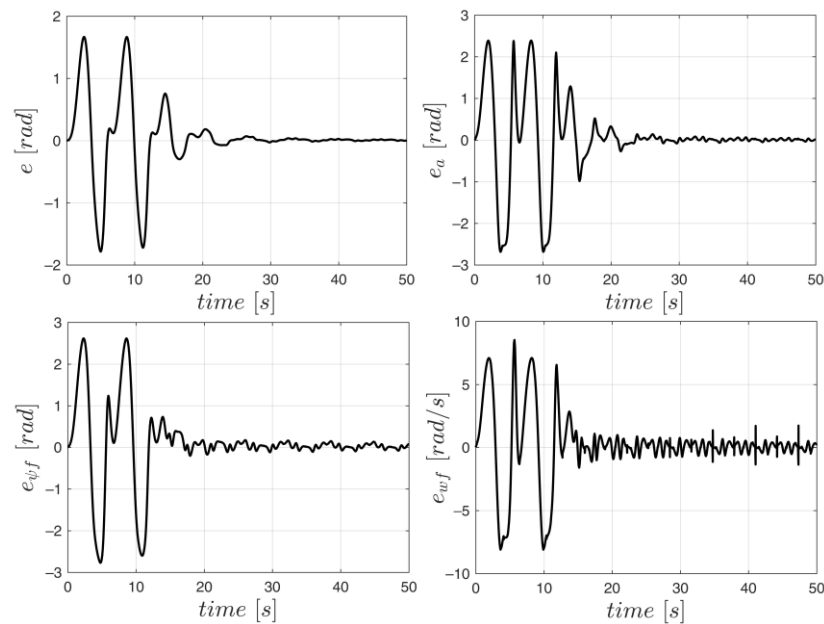


Figure 6. Tracking errors $e, e_a, e_{\psi f}, e_{\omega f}$.

The history of the adaptive parameters referred to the exact values, i.e.,

$$\begin{aligned} \bar{\theta}_a^T &= \hat{\theta}_a^T ./ \begin{bmatrix} J_a & T_a & c_a & b \\ p_1 & p_1 & p_1 & p_1 \end{bmatrix}, \\ \bar{\theta}_m^T &= \hat{\theta}_m^T ./ \begin{bmatrix} J_m & T_m & c_m & p_1 & p_2 \\ k_i & k_i & k_i & k_i & k_i \end{bmatrix}, \quad \bar{p}_{21} = \frac{\hat{p}_{21}}{p_{21}}, \end{aligned} \quad (47)$$

(./ stands for element-wise division) is presented in Figure 7. The adaptive parameters, as demonstrated in Figure 7, approach the exact values if the leakage parameters $\sigma_a, \sigma_m, \sigma_p$ are zero, which proves that the controller is properly derived. This is a typical feature of non-robust adaptive laws in the presence of persistent excitation. But in this case, the adaptation is performed by a pure integrator, and this may result in the uncontrolled drift of the adaptive parameter in a real system. Therefore, small positive leakage parameters $\sigma_a, \sigma_m, \sigma_p$ are used, which stabilize the adaptive laws (43)–(44), but in the case of very small tracking errors, the adaptive parameters approach zero. This is demonstrated in Figure 8. In a real system, the convergence of adaptive parameters to exact values is not as important as robustness. It is critical that the adaptive parameters remain bounded during the whole transient, as demonstrated in Figures 7 and 8. The current also remains inside the constraints imposed by a real motor.

The controller was derived for a plant without damping in the shaft: $\beta = 0$. The same controller was applied for the plant with damping ($\beta = 0.0022$ Nms/rad). It is visible in Figure 9 that the closed-loop system is robust in the presence of such unmodeled damping; the resulting quasi-steady-state error (oscillating slowly) is smaller than four times the encoder resolution. In a real system, we can expect more disruptive factors like discretization, on-line differentiation, unmodeled friction, etc.

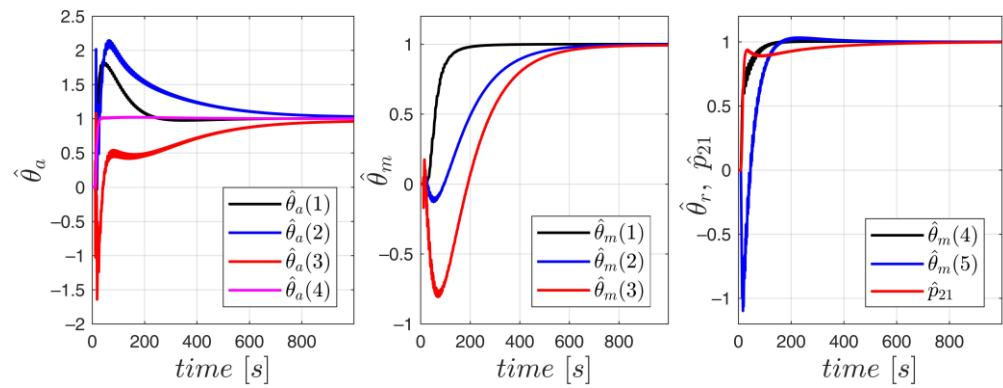


Figure 7. Adaptive parameters referred to exact values for $\sigma_a, \sigma_m, \sigma_p = 0$.

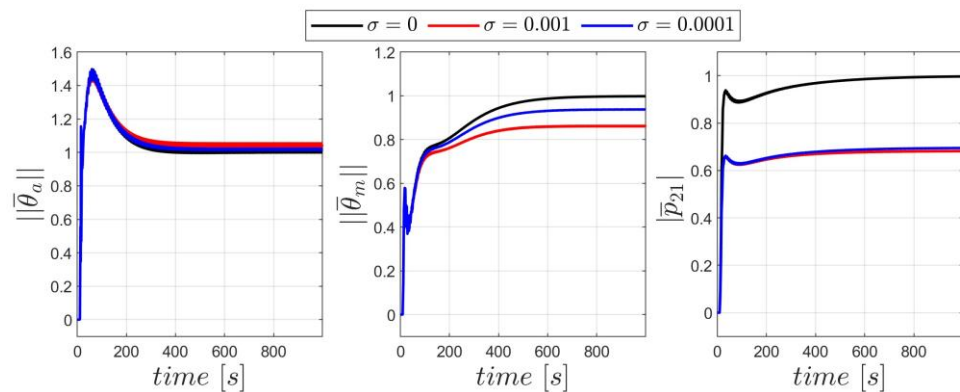


Figure 8. Norm of adaptive parameters for different values of parameters, $\sigma_a = \sigma_m = \sigma_p = \sigma$.

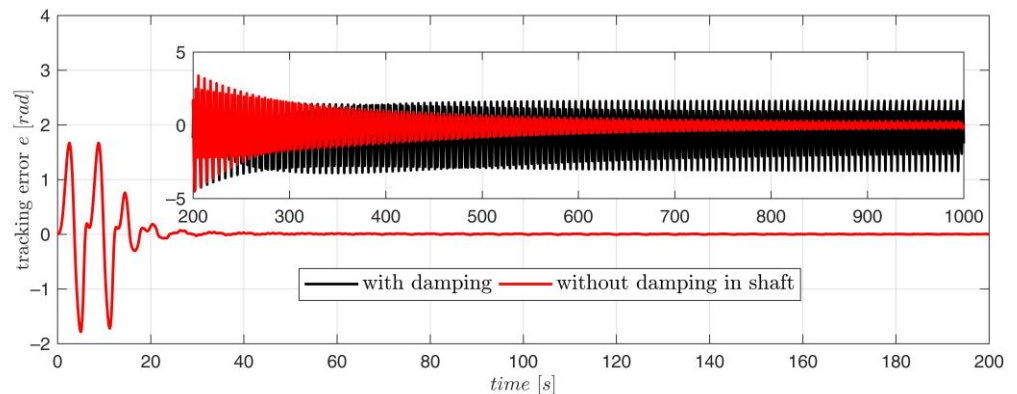


Figure 9. Tracking error for the plant with and without damping.

The subsequent experiments investigated the robustness against possible errors in the stiffness modeling. The selection of the approximating function $S_n(\varphi)$ used in the control algorithm is always an arbitrary decision, and one can wonder how much it influences the closed-loop system's performance. Therefore, we consider three cases: when the stiffness characteristics of the plant is linear ($p_2 = 0$), convex ($p_2 = 0.0704$) and concave ($p_2 = -0.0704$). For each of these three cases, the following models were used in turn in the control algorithm:

- $S_n(\varphi) = 0$, which means that the controller does not attempt to compensate for the stiffness nonlinearity;
- $S_n(\varphi) = \tanh(\varphi)\varphi^2$, which means that the controller is able to compensate for the stiffness nonlinearity exactly, if the adaptive parameters are tuned properly;
- $S_n(\varphi) = \varphi^3$, which means that the controller uses the wrong nonlinear model to compensate for the stiffness nonlinearity of the plant.

The RMSE for the tracking error e calculated for an interval of 20 s during a quasi-steady-state for all nine combinations is presented in Table 3. The initial value of the adaptive parameters was zero for all cases. The plots corresponding to the values presented in Table 3 are given in Figure 10.

Table 3. RMSE [rad] for the tracking error e calculated for an interval of 20 s during a quasi-steady state.

Stiffness Nonlinearity Model Used by the Controller	Plant Stiffness Characteristics: $S(\varphi)=p_1\varphi+p_2S_n(\varphi)=p_1\varphi+p_2\tanh(\varphi)\varphi^2$		
	$p_2=0$	$p_2=-0.0704$	$p_2=0.0704$
$S_n(\varphi) = 0$	0.000861	0.0180	0.00533
$S_n(\varphi) = \tanh(\varphi)\varphi^2$	0.000851	0.0014	0.00051
$S_n(\varphi) = \varphi^3$	0.000847	0.0023	0.00057

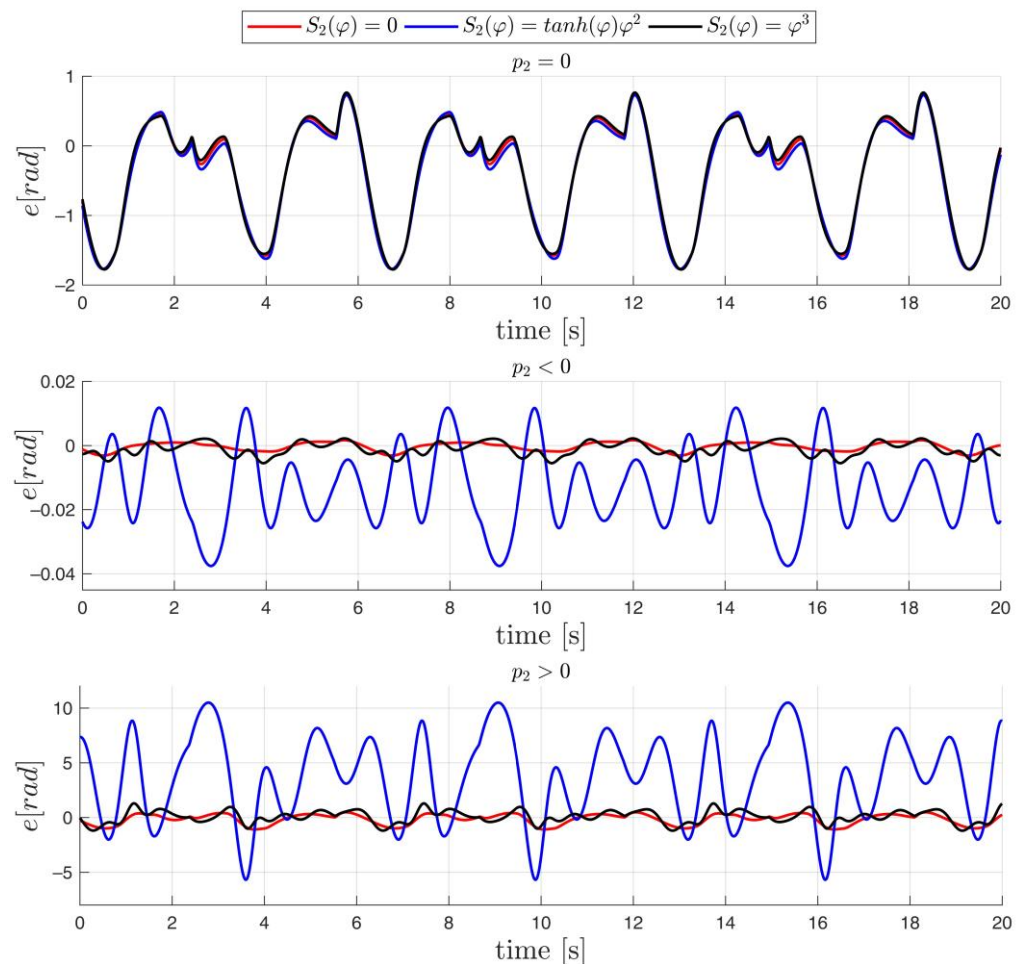


Figure 10. Tracking errors for the nine discussed cases.

If the plant stiffness characteristics are linear, it is not necessary to include a nonlinear model in the controller, so it is not surprising that all three controllers perform similarly. Simply, adaptive parameters corresponding to p_2 are kept close to zero.

If the plant stiffness characteristics are nonlinear, it is smart to include any nonlinear model with similar characteristics. If the model is properly guessed ($S_n(\varphi) = \tanh(\varphi)\varphi^2$), the RMSE is the smallest. If the model is inaccurate ($S_n(\varphi) = \varphi^3$), the RMSE is twice

as big, but the error waveform is similar. If the model neglects the stiffness nonlinearity ($S_n(\varphi) = 0$), the RMSE and the amplitude of the error are 10 times bigger.

4.4. Real Experiments

After carrying out the numerical experiments, the proposed controller was implemented in a real controller with a real plant. Of course, it is impossible to obtain exactly the same results in a real plant like in a simulation. Many additional factors, such as the coupling elasticity, nonlinear current–torque characteristics and unmodeled friction, affect a real plant. The parameters of the controller were the same as those during the simulation (Table 2) except $\sigma_p = 0.01$. Real experiments were carried out for three shafts differing in stiffness (Figure 11). It is assumed that the initial values of the adaptive parameters $\hat{\theta}_a(0)$ are zero. The initial values of the adaptive parameters concerning the motor were taken from the documentation. The initial values of the parameters of the elastic shaft were also equal to zero, so $\hat{p}_{21}(0) = 0$ and $\hat{\theta}_m(0) = [5 \cdot 10^{-4}, 7 \cdot 10^{-2}, 6 \cdot 10^{-4}, 0, 0]$.

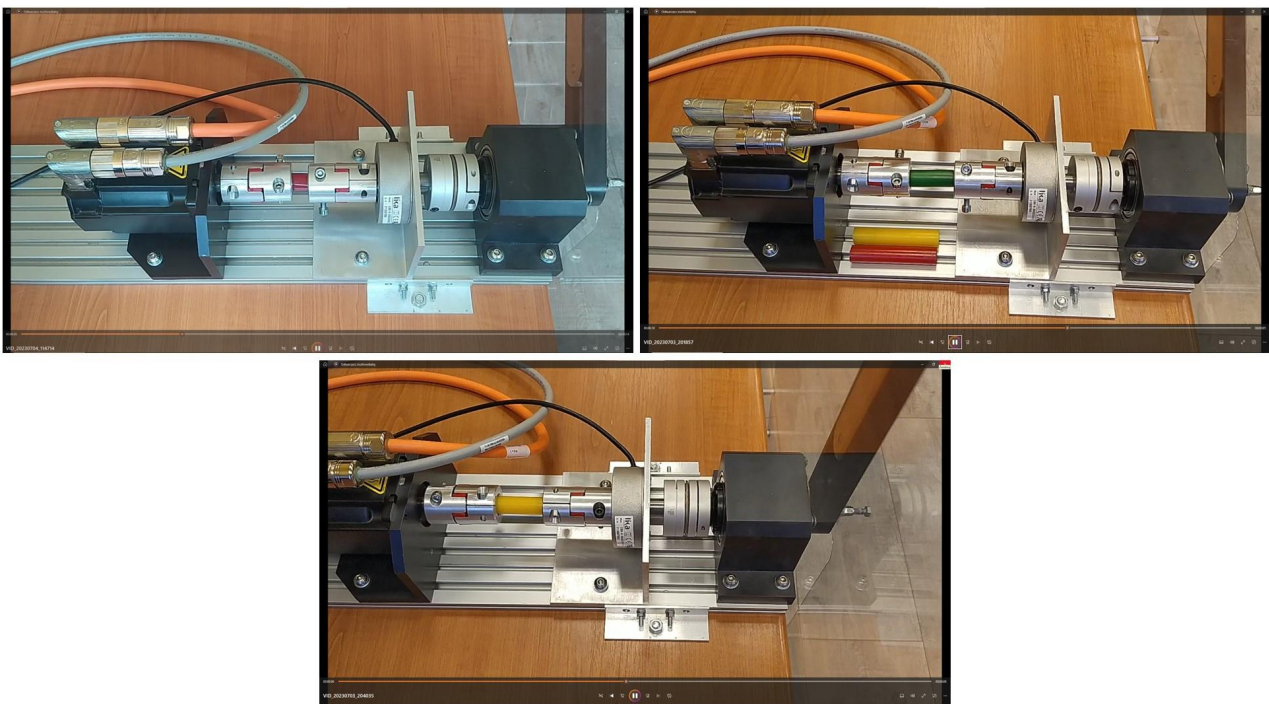


Figure 11. Laboratory stand with three different elastic shafts: soft (red), medium (green) and hard (yellow).

Examples of plots collected during the run of the robotic arm are presented below.

Figures 12–14 demonstrate the tracking error e for different shafts. After the initial part of the transient, the error e reaches a quasi-steady state. In the steady state, the error does not exceed 0.1 [rad] for the soft shaft and 0.05 [rad] for the hard and medium shafts. The adaptive parameters remain bounded, as demonstrated by the plots of $\|\hat{\theta}_a\|$, $\|\hat{\theta}_m\|$, $|\hat{p}_{m21}|$. A comparison of angles φ_a and φ_m indicates that the torsion angle of the shaft reaches up to 3 [rad], so the shaft works in the nonlinear part of the characteristic, as shown in Figure 2b. The upper figures demonstrate the complete tracking history: the transient, the period of fast-changing adaptive parameters and the quasi-steady state with almost constant adaptive parameters. The lower figures present the initial period of the position and current time history. After 15–30 s, the plots of the desired and actual values overlap.

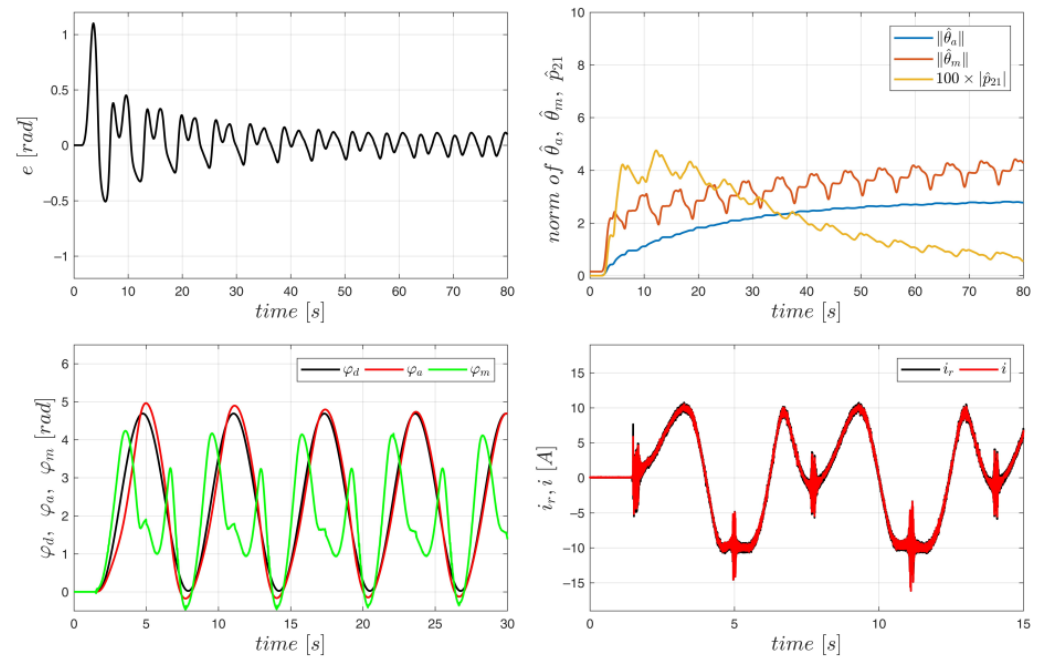


Figure 12. Tracking errors e , norm of adaptive parameters, reference trajectory φ_d , angles φ_a , φ_m , reference i_r , and real motor current i for the soft (red) shaft.

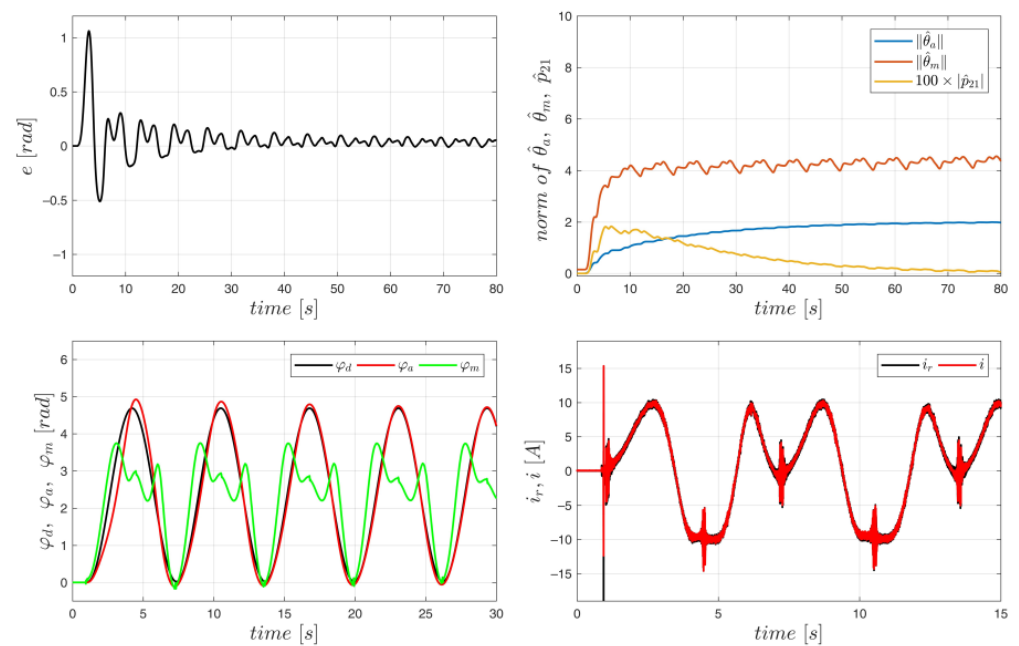


Figure 13. Tracking errors e , norm of adaptive parameters, reference trajectory φ_d , angles φ_a , φ_m , reference i_r , and real motor current i for the medium (green) shaft.

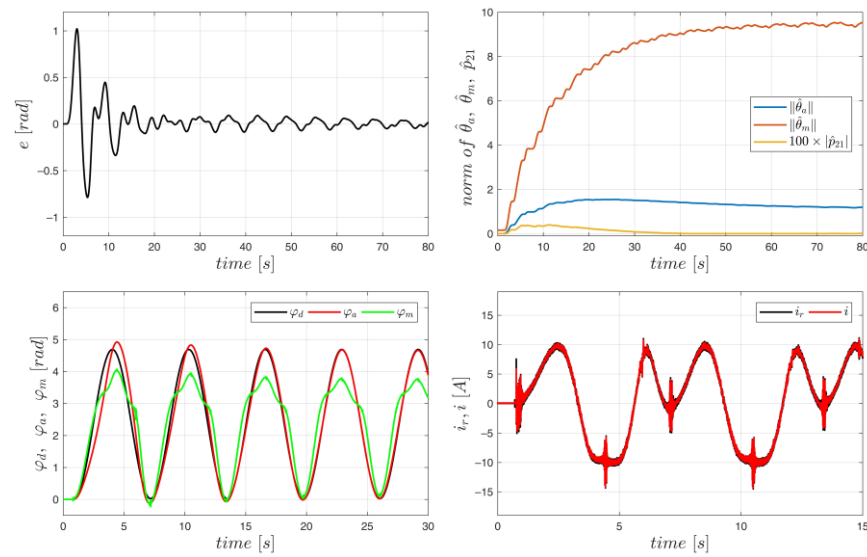


Figure 14. Tracking errors e , norm of adaptive parameters, reference trajectory φ_d , angles φ_a , φ_m , reference i_r and real motor current i for the hard (yellow) shaft.

4.5. Comparison with Previous Results

The controller derived in this paper (denoted by AB) was compared with the other one (denoted as PP):

$$i_r = -k_1(\varphi_a - \varphi_d) - k_2(\omega_a - \dot{\varphi}_d) - k_3\left(\varphi_m - \varphi_d - \frac{b}{p}\sin(\varphi_d)\right) - k_4\left(\omega_r - \dot{\varphi}_d - \frac{b}{p}\cos(\varphi_d)\dot{\varphi}_d\right) + b\sin(\varphi_a). \tag{48}$$

Controller PP is derived from a linear model of the drive. Gains $k_1 = 3.57, k_2 = 0.42, k_3 = 0.20, k_4 = 0.01$ were selected to place the closed-loop poles at $[-20, -30, -40, -50]$. This control concept was presented in [42] and modified in [41]. Our modification relies on using pole placement to calculate the gains. The original approach, based on the inertia of the load, provides a very slow response for the drive. The selection of the poles' positions was motivated by obtaining a fast a-periodical transient with gains that are acceptable in a real plant, as was achieved using the AB controller. Both controllers, PP and AB, use the same measured outputs of the drive. Controller PP is not an adaptive one, and its operation without accurate drive parameters is impossible. The operation of the controllers was compared using reference signals, as presented in Figure 15. First, simulations for the medium shaft ($p_1 = 0.731$) were performed for different stiffness characteristics: linear ($p_2 = 0$) and nonlinear ($p_2 = -0.0704$). The results are presented in Table 4.

Table 4. Tracking RMSE [rad] for different stiffnesses.

RMSE for 1 Revolution	PP	AB
Linear stiffness	0.0064	0.0063
Nonlinear stiffness	0.0221	0.0063

As follows from the data presented in Table 3, if the stiffness characteristics are linear, the operation of both controllers is similar. In the case of nonlinear stiffness, the controller derived here (AB) outperforms PP, achieving an RMSE that is three times smaller. Next, both controllers were tested with a real drive. As demonstrated in Figure 15, the controller derived here provides an amplitude for the quasi-steady-state tracking error that is twice as small. Moreover, the tracking accuracy is continuously improved when the adaptation goes on.

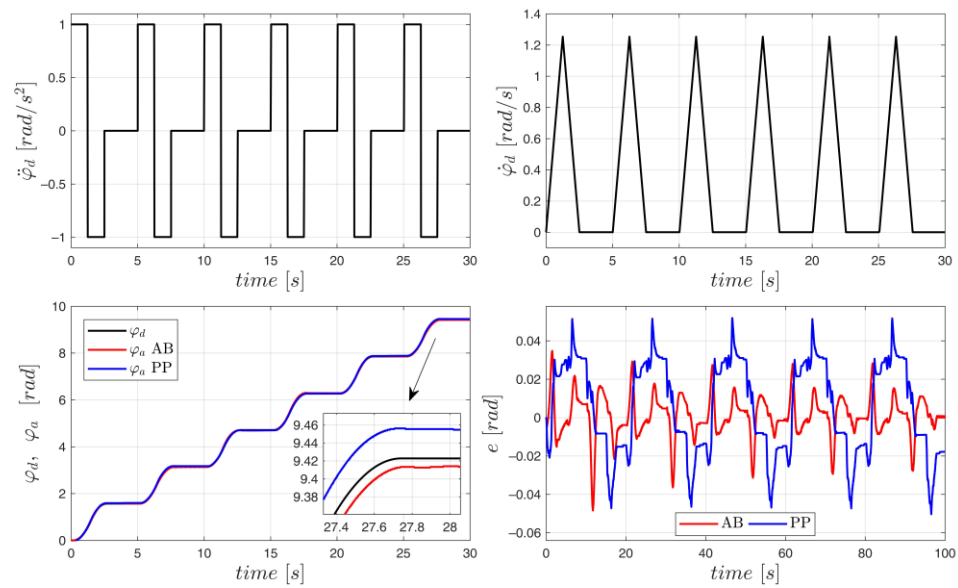


Figure 15. Desired acceleration $\ddot{\varphi}_d$, velocity $\dot{\varphi}_d$, position φ_d , load position φ_a and tracking error e for the AB and PP controllers.

The tracking accuracy of the PP controller deteriorates if the nonlinear stiffness appears (despite all other parameters being known exactly), and the adaptive controller AB keeps the tracking error low.

Also, for the real plant, when many parameters are not known precisely and many other factors deteriorate the performance of both controllers, the AB controller outperforms the PP controller, offering a better tracking quality with the same measurements and motor current constrains.

It was checked whether the operation of each controller could be improved by better selection of the parameters. For the same reference as in Figure 15, and taking into account encoder quantization, each controller was optimized using the Matlab Global Optimization toolbox from Matlab ver. 2020a (procedure gamultiobj). For the PP controllers, the decision parameters were the poles' positions (each inside the interval $[-200, -10]$), and for the AB controller, the parameters were $\tau, k_a, k_\psi, k_\omega$ (within $[0.01, 200]$). The objectives were the tracking RMSE (as in Table 4) and $\int_{t_0}^{t_0+t_r} i_r^2(t)dt$, where t_r is the time required to perform a revolution of 360° . Multicriterial genetic optimization was performed with the parameters of PopulationSize = 100 and MaxGenerations = 50. The obtained Pareto fronts are presented in Figure 16.

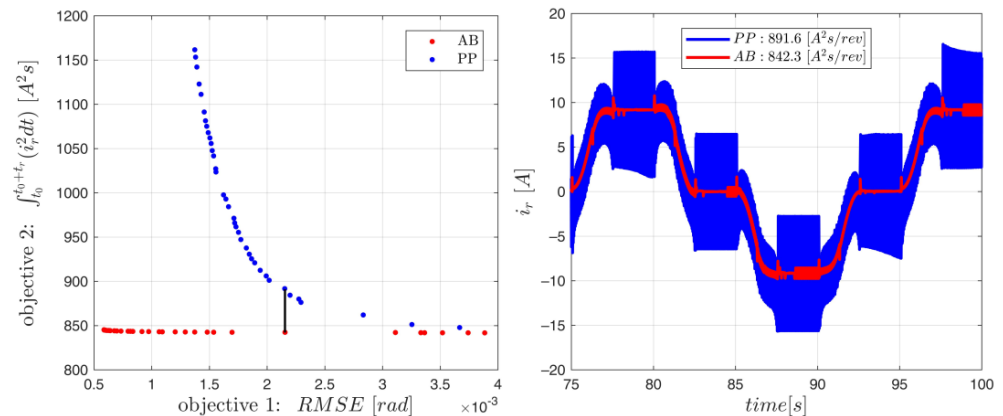


Figure 16. Pareto fronts resulting from multicriterial optimization of controllers AB and PP (left). Current during quasi-steady-state operation corresponding to two indicated points of Pareto fronts (right).

It is visible that, if the PP controller is used, decreasing the tracking error requires much higher energy consumption. In addition, smaller values of the tracking RMSE are unavailable because of current constraints, and the AB controller achieves a smaller tracking RMSE with practically the same current. Also, the comparison of the current plots corresponding to the same tracking RMSE proves the superiority of the AB controller over the PP one.

5. Conclusions

A new, adaptive, position-tracking controller for a two-mass drive with a flexible joint possessing a nonlinear stiffness characteristic is presented. The control was derived in a strictly mathematical manner and tested via implementation in a DSP system controlling a real drive.

The derived nonlinear adaptive controller ensures accurate tracking of the desired position despite the unknown parameters of the motor and the load. It operates correctly, even if the applied joint is very flexible, allowing for high torsion angle values. It is shown that taking into account the nonlinear stiffness characteristics allows for a several-fold reduction in the tracking error, compared to the results obtained assuming that the stiffness coefficient is constant and that the transmitted torque is proportional to the torsion angle.

The application of several smart design techniques, such as using an augmented tracking error, virtual control command filtering and robust adaptive laws, allowed for the simplification of the controller and enabled its implementation in a real plant using a DSP processor. It was demonstrated that the implemented controller is robust against discretization and modeling errors, concerning friction, shaft damping, current-loop dynamics, etc. Second-order differentiator filters used to compute virtual control derivatives enabled smoother control, although this approach complicated the derivation compared to the first-order filter technique. The experiment proved that the adaptive mechanism is strong enough to cope with changing the flexible joint to another with different characteristics.

Of course, some decisions, like the type of adaptive laws used, tuning techniques, etc., are arbitrary, and further research can be conducted on their impact on the overall system performance.

Author Contributions: Main idea, J.K.; methodology, J.K. and P.M.; simulations, M.J.; validation, J.K. and P.M.; writing—original draft preparation, J.K., P.M. and M.J.; writing—review and editing, J.K.; visualization, M.J. and P.M. All authors have read and agreed to the published version of the manuscript.

Funding: This research was funded by the Politechnika Łódzka (Lodz University of Technology).

Data Availability Statement: Dataset available on request from the authors. The data are not publicly available due to [technical limitation—raw real data size over 10GB].

Conflicts of Interest: The authors declare no conflicts of interest.

Appendix A

In the first step, we formulate Lemma A1, describing the properties of the proposed linear second-order filters.

Lemma A1. *For a linear system described by the equation*

$$\dot{x} = Ax + Bu \quad (\text{A1})$$

where

$$A = \begin{bmatrix} 0 & 1 \\ -\frac{1}{\tau^2} & -\frac{2}{\tau} \end{bmatrix}, B = \begin{bmatrix} 0 \\ 1 \end{bmatrix}, \tau > 0$$

1. Matrix A has a double eigenvalue $-\frac{1}{\tau}$.
2. For any $k_0 > 0$, there exists $\tau_{k_0} > 0$ such that, for any $0 < \tau < \tau_{k_0}$, matrix $A + \frac{k_0}{2} I_2$ is stable.
3. For any $w > 0$, there exists $\tau_w > 0$ such that, for any $0 < \tau < \tau_w$, there exists a positive definite solution Q for the Lyapunov equation:

$$\left(A^T + \frac{k_0}{2} I_2\right)Q + Q\left(A + \frac{k_0}{2} I_2\right) = -wI_2 \tag{A2}$$

4. For any $C > 0$ and $w > \frac{1}{2}$, there exists $\tau_{Cw} > 0$ such that, for any $0 < \tau < \tau_{Cw}$, the matrix

$$R = \left(A^T + \frac{k_0}{2} I_2\right)Q + Q\left(A + \frac{k_0}{2} I_2\right) + CQB B^T Q + \frac{1}{2} I_2 \tag{A3}$$

is negative definite.

Proof of Lemma A1.

1. The eigenvalues of matrix A are the roots of the characteristic polynomial

$$M(s) = \det(sI_2 - A) = \det \begin{bmatrix} s & -1 \\ \frac{1}{\tau^2} & s + \frac{2}{\tau} \end{bmatrix} = s^2 + \frac{2}{\tau}s + \frac{1}{\tau^2} = \left(s + \frac{1}{\tau}\right)^2. \tag{A4}$$

Polynomial (A4) possesses a double root $s = -\frac{1}{\tau}$, so matrix A has a double eigenvalue $-\frac{1}{\tau}$.

2. The characteristic polynomial of the matrix

$$A_1 = A + \frac{k_0}{2} I_2 = \begin{bmatrix} \frac{k_0}{2} & 1 \\ -\frac{1}{\tau^2} & \frac{k_0}{2} - \frac{2}{\tau} \end{bmatrix} \tag{A5}$$

is

$$\begin{aligned} M(s) = \det(sI_2 - A_1) &= \begin{vmatrix} s - \frac{k_0}{2} & -1 \\ \frac{1}{\tau^2} & s + \frac{2}{\tau} - \frac{k_0}{2} \end{vmatrix} = \left(s - \frac{k_0}{2}\right)\left(s + \frac{2}{\tau} - \frac{k_0}{2}\right) + \frac{1}{\tau^2} \\ &= s^2 + \left(\frac{2}{\tau} - k_0\right)s + \frac{(k_0\tau - 2)^2}{4\tau^2} = \left(s - \frac{k_0\tau - 2}{2\tau}\right)^2 \end{aligned} \tag{A6}$$

Polynomial (A6) possesses a double root $s = \frac{k_0\tau - 2}{2\tau}$, which is stable if the condition $k_0\tau - 2 < 0$ is fulfilled. So, $\tau_{k_0} = \frac{2}{k_0}$.

3. If the condition $\tau k_0 < 2$ is met, the matrix $\left(A + \frac{k_0}{2} I_2\right)$ is stable, so for any $w > 0$, there exists a unique positive definite solution $Q = \begin{bmatrix} q_1 & q_2 \\ q_2 & q_3 \end{bmatrix}$ for the Lyapunov equation:

$$\left(A^T + \frac{k_0}{2} I_2\right)Q + Q\left(A + \frac{k_0}{2} I_2\right) = -wI_2 \tag{A7}$$

which has the form

$$\begin{cases} q_2 = w\tau \frac{(k_0\tau^2 - 4\tau - k_0)}{(\tau k_0 - 2)^3} \\ q_3 = w\tau \frac{((k_0\tau^2 - 4\tau - k_0)(k_0^2\tau^2 - 2k_0\tau + 2) - \tau(\tau k_0 - 2)^3)}{k_0(\tau k_0 - 2)^3} \\ q_1 = -\frac{w(k_0\tau^2 - 4\tau - k_0)}{(\tau k_0 - 2)^2} + \frac{1}{\tau} w \frac{(k_0\tau^2 - 4\tau - k_0)(k_0^2\tau^2 - 2k_0\tau + 2) - \tau(\tau k_0 - 2)^3}{k_0(\tau k_0 - 2)^3} \end{cases}. \tag{A8}$$

So, $\tau_w = \tau_{k_0}$.

4. Matrix QBB^TQ has the form

$$P = QBB^TQ = \begin{bmatrix} q_1 & q_2 \\ q_2 & q_3 \end{bmatrix} \begin{bmatrix} 0 \\ 1 \end{bmatrix} \begin{bmatrix} 0 & 1 \end{bmatrix} \begin{bmatrix} q_1 & q_2 \\ q_2 & q_3 \end{bmatrix} = \begin{bmatrix} q_2 \\ q_3 \end{bmatrix} \begin{bmatrix} q_2 & q_3 \end{bmatrix} = \begin{bmatrix} q_2^2 & q_2q_3 \\ q_2q_3 & q_3^2 \end{bmatrix}. \quad (\text{A9})$$

The eigenvalues of matrix P can be determined from the characteristic equation

$$\det(sI_2 - P) = \begin{vmatrix} s - q_2^2 & -q_2q_3 \\ -q_2q_3 & s - q_3^2 \end{vmatrix} = (s - q_2^2)(s - q_3^2) - q_2^2q_3^2 = s^2 - (q_2^2 + q_3^2)s = s(s - (q_2^2 + q_3^2)) = 0. \quad (\text{A10})$$

The minimal eigenvalue of P equals zero, and the maximal eigenvalue λ_M equals

$$\begin{aligned} \lambda_M(P) &= q_2^2 + q_3^2 = \left(w\tau \frac{(k_0\tau^2 - 4\tau - k_0)}{(\tau k_0 - 2)^3} \right)^2 \\ &\quad + \left(w\tau \frac{((k_0\tau^2 - 4\tau - k_0)(k_0^2\tau^2 - 2k_0\tau + 2) - \tau(\tau k_0 - 2)^3)}{k_0(\tau k_0 - 2)^3} \right)^2 \\ &= w^2\tau^2 \left(\left(\frac{k_0(k_0\tau^2 - 4\tau - k_0)}{k_0(\tau k_0 - 2)^3} \right)^2 \right. \\ &\quad \left. + \left(\frac{((k_0\tau^2 - 4\tau - k_0)(k_0^2\tau^2 - 2k_0\tau + 2) - \tau(\tau k_0 - 2)^3)}{k_0(\tau k_0 - 2)^3} \right)^2 \right) \\ &= w^2\tau^2 \frac{(k_0\tau^2 - 4\tau - k_0)^2}{k_0^2(\tau k_0 - 2)^6} \left[k_0^2 \right. \\ &\quad \left. + \left((k_0^2\tau^2 - 2k_0\tau + 2) - \tau(\tau k_0 - 2)^3 \right)^2 \right] = w^2\tau^2 f(\tau) \end{aligned} \quad (\text{A11})$$

$$\text{where } f(\tau) = \frac{(k_0\tau^2 - 4\tau - k_0)^2}{k_0^2(\tau k_0 - 2)^6} \left[k_0^2 + \left((k_0^2\tau^2 - 2k_0\tau + 2) - \tau(\tau k_0 - 2)^3 \right)^2 \right].$$

For any $\epsilon > 0$ and $\tau k_0 < 2 - \epsilon$, the function $f(\tau)$ is bounded by $F = f\left(\frac{2-\epsilon}{k_0}\right) > 0$. In addition, $\tau \rightarrow 0$ decreases monotonically to $f(0) = \frac{1}{2^6} [k_0^2 + 2]$, so

$$\lim_{\tau \rightarrow 0} \lambda_M(P) = w^2 \lim_{\tau \rightarrow 0} \tau^2 f(\tau) = 0. \quad (\text{A12})$$

Matrix $R = \left(A^T + \frac{k_0}{2}I_2\right)Q + Q\left(A + \frac{k_0}{2}I_2\right) + CQBB^TQ + \frac{1}{2}I_2 = CQBB^TQ + \left(\frac{1}{2} - w\right)I_2$ is negative definite if the condition

$$C\lambda_M(QB_1B_1^TQ) + \left(\frac{1}{2} - w\right) = Cw^2\tau^2f(\tau) + \left(\frac{1}{2} - w\right) < 0 \quad (\text{A13})$$

is met. Since the function $f(\tau)$ is bounded, the inequality

$$Cw^2\tau^2f(\tau) + \left(\frac{1}{2} - w\right) \leq Cw^2\tau^2F + \left(\frac{1}{2} - w\right) \quad (\text{A14})$$

is true. If the inequality $\tau^2 < \frac{w-\frac{1}{2}}{Cw^2F}$ is true, inequality (A13) is true, so $\tau_{Cw} = \min\left\{\frac{2-\epsilon}{k_0}, \sqrt{\frac{w-\frac{1}{2}}{Cw^2F}}\right\}$.
□

Lemma A2. For any scalar χ , column vectors α and β and any $\epsilon > 0$, we have $\chi\alpha^T\beta + \chi\beta^T\alpha \leq \frac{\chi^2}{\epsilon}(\alpha^T\beta)^2 + \epsilon = \frac{\chi^2}{\epsilon}\alpha^T\beta\beta^T\alpha + \epsilon = \frac{\chi^2}{\epsilon}\beta^T\alpha\alpha^T\beta + \epsilon$.

Proof of Lemma A2. Indeed, $2\chi\alpha^T\beta = \frac{\chi^2}{\epsilon}(\alpha^T\beta)^2 - \left(\frac{\chi}{\sqrt{\epsilon}}\alpha^T\beta - \sqrt{\epsilon}\right)^2 + \epsilon \leq \frac{\chi^2}{\epsilon}(\alpha^T\beta)^2 + \epsilon$.
□

Proof of Theorem1. We consider the Lyapunov function defined by Equation (42). Let us repeat that the symmetric positive definite matrices Q_1 and Q_2 are not specified yet and are not used in the designed controller equations.

The derivative of the Lyapunov function along the system trajectories is given by

$$\begin{aligned} \dot{V} = & e_a \frac{J_a}{\tau_0 p_1} \dot{e}_a + e_{\psi f} \dot{e}_{\psi f} + e_{\omega f} \frac{J_m}{k_i} \dot{e}_{\omega f} + \tilde{\theta}_a^T \Gamma_a^{-1} \dot{\tilde{\theta}}_a + \frac{1}{\gamma_p} \tilde{p}_{21} \dot{\tilde{p}}_{21} + \tilde{\theta}_m^T \Gamma_m^{-1} \dot{\tilde{\theta}}_m \\ & + \dot{\rho}_{\tau 1}^T Q_1 \rho_{\tau 1} + \rho_{\tau 1}^T Q_1 \dot{\rho}_{\tau 1} + \dot{\rho}_{\tau 2}^T Q_2 \rho_{\tau 2} + \rho_{\tau 2}^T Q_2 \dot{\rho}_{\tau 2}. \end{aligned} \tag{A15}$$

After substituting Equations (20), (23), (32), (35) and (41) into (A15), we obtain

$$\begin{aligned} \dot{V} = & e_a \left(-k_a e_a + \tilde{\theta}_a^T \xi_a + e_{\psi f} + \rho_{\psi} - \tilde{p}_{21} S_n(\varphi) - \frac{1}{2} e_a \right) \\ & + e_{\psi f} \left(-k_{\psi} e_{\psi f} - e_a + \left(1 + \hat{p}_{21} \frac{dS_n(\varphi)}{d\varphi} \right) (e_{\omega f} + \rho_{\omega}) \right. \\ & \left. - \frac{1}{2} \left(1 + \hat{p}_{21} \frac{dS_n(\varphi)}{d\varphi} \right)^2 e_{\psi f} \right) \\ & + e_{\omega f} \left(-k_{\omega} e_{\omega f} + \tilde{\theta}_m^T \xi_m - \left(1 + \hat{p}_{21} \frac{dS_n(\varphi)}{d\varphi} \right) e_{\psi f} \right) + \tilde{\theta}_a^T \Gamma_a^{-1} \dot{\tilde{\theta}}_a \\ & + \frac{1}{\gamma_p} \tilde{p}_{21} \dot{\tilde{p}}_{21} + \tilde{\theta}_m^T \Gamma_m^{-1} \dot{\tilde{\theta}}_m + \rho_{\tau 1}^T A_{\rho 1}^T Q_1 \rho_{\tau 1} + \rho_{\tau 1}^T Q_1 A_{\rho 1} \rho_{\tau 1} + B_{\rho 1}^T Q_1 \rho_{\tau 1} H_{1\tau} \\ & + \rho_{\tau 1}^T Q_1 B_{\rho 1} H_{1\tau} + \rho_{\tau 2}^T A_{\rho 2}^T Q_2 \rho_{\tau 2} + \rho_{\tau 2}^T Q_2 A_{\rho 2} \rho_{\tau 2} + B_{\rho 2}^T Q_2 \rho_{\tau 2} H_{2\tau} \\ & + \rho_{\tau 2}^T Q_2 B_{\rho 2} H_{2\tau}. \end{aligned} \tag{A16}$$

Components $B_{\rho i}^T Q_i \rho_{\tau i} H_{i\tau} + \rho_{\tau i}^T Q_i B_{\rho i} H_{i\tau}$, $i = 1, 2$, which are linear in $\rho_{\tau i}$, must be constrained by quadratic forms with respect to $\rho_{\tau i}$. This is performed by applying Lemma A2 to each of the components $i = 1, 2$. Also, taking into account that all parameters are constant, we have $\dot{\tilde{\theta}}_a = -\dot{\hat{\theta}}_a$, $\dot{\tilde{\theta}}_m = -\dot{\hat{\theta}}_m$, $\dot{\tilde{p}}_{21} = -\dot{\hat{p}}_{21}$. Hence, Equation (A16) can be reduced to obtain an inequality:

$$\begin{aligned} \dot{V} \leq & -k_a e_a^2 - k_{\psi} e_{\psi f}^2 - k_{\omega} e_{\omega f}^2 - \frac{1}{2} (e_a - \rho_{\psi})^2 + \frac{1}{2} \rho_{\psi}^2 + \frac{1}{2} \rho_{\omega}^2 + \\ & - \frac{1}{2} \left(\left(1 + \hat{p}_{21} \frac{dS_2(\varphi)}{d\varphi} \right) e_{\psi f} - \rho_{\omega} \right)^2 + \tilde{\theta}_m^T \left(\xi_m e_{\omega f} - \Gamma_m^{-1} \dot{\tilde{\theta}}_m \right) + \\ & - \tilde{p}_{21} \left(\frac{1}{\gamma_p} \dot{\tilde{p}}_{21} + S_n(\varphi) e_a \right) + \tilde{\theta}_a^T \left(\xi_a e_a - \Gamma_a^{-1} \dot{\tilde{\theta}}_a \right) \\ & + \rho_{\tau 1}^T A_{\rho 1}^T Q_1 \rho_{\tau 1} + \rho_{\tau 1}^T Q_1 A_{\rho 1} \rho_{\tau 1} + \frac{H_{1\tau}^2}{\varepsilon_1} \rho_{\tau 1}^T Q_1 B_{\rho 1} B_{\rho 1}^T Q_1 \rho_{\tau 1} + \varepsilon_1 \\ & + \rho_{\tau 2}^T A_{\rho 2}^T Q_2 \rho_{\tau 2} + \rho_{\tau 2}^T Q_2 A_{\rho 2} \rho_{\tau 2} + \frac{H_{2\tau}^2}{\varepsilon_2} \rho_{\tau 2}^T Q_2 B_{\rho 2} B_{\rho 2}^T Q_2 \rho_{\tau 2} + \varepsilon_2 \end{aligned} \tag{A17}$$

for any $\varepsilon_1 > 0$ and $\varepsilon_2 > 0$.

After substituting the adaptive laws (43) and (44) into (A17), we obtain

$$\begin{aligned} \dot{V} = & -k_a e_a^2 - k_{\psi} e_{\psi f}^2 - k_{\omega} e_{\omega f}^2 - \frac{1}{2} (e_a - \rho_{\psi})^2 + \frac{1}{2} \rho_{\psi}^2 + \frac{1}{2} \rho_{\omega}^2 \\ & - \frac{1}{2} \left(\left(1 + \hat{p}_{21} \frac{dS_2(\varphi)}{d\varphi} \right) e_{\psi f} - \rho_{\omega} \right)^2 + \sigma_m \tilde{\theta}_m \dot{\hat{\theta}}_m + \sigma_a \tilde{\theta}_a \dot{\hat{\theta}}_a \\ & - \tilde{p}_{21} \left(Proj_{p^m, p^M}(\gamma, \hat{p}_{21}) + S_n(\varphi) e_a \right) + \rho_{\tau 1}^T A_{\rho 1}^T Q_1 \rho_{\tau 1} + \rho_{\tau 1}^T Q_1 A_{\rho 1} \rho_{\tau 1} \\ & + \frac{H_{1\tau}^2}{\varepsilon_1} \rho_{\tau 1}^T Q_1 B_{\rho 1} B_{\rho 1}^T Q_1 \rho_{\tau 1} + \varepsilon_1 + \rho_{\tau 2}^T A_{\rho 2}^T Q_2 \rho_{\tau 2} + \rho_{\tau 2}^T Q_2 A_{\rho 2} \rho_{\tau 2} \\ & + \frac{H_{2\tau}^2}{\varepsilon_2} \rho_{\tau 2}^T Q_2 B_{\rho 2} B_{\rho 2}^T Q_2 \rho_{\tau 2} + \varepsilon_2. \end{aligned} \tag{A18}$$

Using (44) and (45), we obtain

$$\begin{aligned}
 & -\tilde{p}_{21} \left(Proj_{p^m, p^M}(\gamma, \hat{p}_{21}) + S_n(\varphi)e_a \right) \\
 & = \tilde{p}_{21} \left(-S_n(\varphi)e_a - \sigma_P \hat{p}_{21} - Proj_{p^m, p^M}(\gamma, \hat{p}_{21}) \right) + \sigma_P \tilde{p}_{21} \hat{p}_{21} \\
 & = \tilde{p}_{21} \left(\gamma - Proj_{p^m, p^M}(\gamma, \hat{p}_{21}) \right) + \sigma_P \tilde{p}_{21} \hat{p}_{21} \leq \sigma_P \tilde{p}_{21} \hat{p}_{21}.
 \end{aligned} \tag{A19}$$

Because

$$\tilde{\theta}_m \hat{\theta}_m \leq -\frac{1}{2} \tilde{\theta}_m^T \tilde{\theta}_m + \frac{1}{2} \theta_m^T \theta_m, \quad \tilde{\theta}_a \hat{\theta}_a \leq -\frac{1}{2} \tilde{\theta}_a^T \tilde{\theta}_a + \frac{1}{2} \theta_a^T \theta_a, \quad \tilde{p}_{21} \hat{p}_{21} \leq -\frac{1}{2} \tilde{p}_{21}^2 + \frac{1}{2} p_{21}^2, \tag{A20}$$

it follows from (A19) and (A20) that

$$\begin{aligned}
 \dot{V} & \leq -k_a e_a^2 - k_\psi e_{\psi_f}^2 - k_\omega e_{\omega_f}^2 - \frac{\sigma_a}{2} \tilde{\theta}_a^T \tilde{\theta}_a - \frac{\sigma_m}{2} \tilde{\theta}_m^T \tilde{\theta}_m - \frac{\sigma_P}{2} \tilde{p}_{21}^2 + \frac{\sigma_m}{2} \theta_m^T \theta_m + \frac{\sigma_a}{2} \theta_a^T \theta_a \\
 & + \frac{\sigma_P}{2} p_{21}^2 + \rho_{\tau_1}^T A_{\rho_1}^T Q_1 \rho_{\tau_1} + \rho_{\tau_1}^T Q_1 A_{\rho_1} \rho_{\tau_1} + \frac{H_{1\tau}^2}{\varepsilon_1} \rho_{\tau_1}^T Q_1 B_{\rho_1} B_{\rho_1}^T Q_1 \rho_{\tau_1} + \varepsilon_1 \\
 & + \rho_{\tau_2}^T A_{\rho_2}^T Q_2 \rho_{\tau_2} + \rho_{\tau_2}^T Q_2 A_{\rho_2} \rho_{\tau_2} + \frac{H_{2\tau}^2}{\varepsilon_2} \rho_{\tau_2}^T Q_2 B_{\rho_2} B_{\rho_2}^T Q_2 \rho_{\tau_2} + \varepsilon_2 \\
 & + \frac{1}{2} \rho_{\tau_1}^T \rho_{\tau_1} + \frac{1}{2} \rho_{\tau_2}^T \rho_{\tau_2}.
 \end{aligned} \tag{A21}$$

Let us assume that the desired trajectory is smooth enough in the sense that φ_d and its derivatives are bounded. Therefore, there exists $R_0 > 0$ such that, for any $t \geq 0$, the five $(\varphi_d, \dot{\varphi}_d, \ddot{\varphi}_d, \varphi_d^{(3)}, \varphi_d^{(4)})$ belong to a compact set

$$\mathbf{B}_0 := \left\{ (\varphi_d, \dot{\varphi}_d, \ddot{\varphi}_d, \varphi_d^{(3)}, \varphi_d^{(4)}) : \varphi_d^2 + \dot{\varphi}_d^2 + \ddot{\varphi}_d^2 + (\varphi_d^{(3)})^2 + (\varphi_d^{(4)})^2 \leq R_0^2 \right\} \subset \mathbf{R}^5.$$

Let us consider any arbitrary but specified $r > 0$ and any trajectory $(e_a, e_{\psi_f}, e_{\omega_f}, \tilde{\theta}_a, \tilde{\theta}_m, \tilde{p}_{21}, \rho_{\tau_1}, \rho_{\tau_2})$ starting inside the compact set $\mathbf{B}_1 := \left\{ (e_a, e_{\psi_f}, e_{\omega_f}, \tilde{\theta}_a, \tilde{\theta}_m, \tilde{p}_{21}, \rho_{\tau_1}, \rho_{\tau_2}) : V \leq 2r \right\} \subset \mathbf{R}^{17}$.

Functions $H_{1\tau}$ and $H_{2\tau}$ defined by (20) and (32) are bounded as continuous functions of $\varphi_d, \dot{\varphi}_d, \ddot{\varphi}_d, \varphi_d^{(3)}, \varphi_d^{(4)}, e_a, e_{\psi_f}, e_{\omega_f}, \tilde{\theta}_a, \tilde{\theta}_m, \tilde{p}_{21}, \rho_{\tau_1}, \rho_{\tau_2}$ on a compact set $\mathbf{B}_0 \times \mathbf{B}_1 \subset \mathbf{R}^{22}$; therefore, if the argument $*$ $\in \mathbf{B}_0 \times \mathbf{B}_1$, then $|H_{1\tau}(*)| \leq M_1$ and $|H_{2\tau}(*)| \leq M_2$. For sufficiently small τ_1 and τ_2 , constraints M_1 and M_2 do not depend on τ_1 and τ_2 .

Hence, by calculating the Lyapunov function derivative along any trajectory in \mathbf{B}_1 , we have

$$\begin{aligned}
 \dot{V} & \leq -\frac{2k_a \tau_0 p_1}{J_a} \frac{J_a}{2\tau_0 p_1} e_a^2 - 2k_\psi \frac{1}{2} e_{\psi_f}^2 - \frac{2k_i k_\omega}{J_m} \frac{J_m}{2k_i} e_{\omega_f}^2 - \frac{\sigma_a}{2\lambda_M(\Gamma_a^{-1})} \tilde{\theta}_a^T \Gamma_a^{-1} \tilde{\theta}_a \\
 & - \frac{\sigma_m}{2\lambda_M(\Gamma_m^{-1})} \tilde{\theta}_m^T \Gamma_m^{-1} \tilde{\theta}_m - \frac{\gamma p \sigma_P}{2} \frac{1}{\gamma_p} \tilde{p}_{21}^2 \\
 & + \rho_{\tau_1}^T \left(A_{\rho_1}^T Q_1 + Q_1 A_{\rho_1} + \frac{M_1^2}{\varepsilon_1} Q_1 B_{\rho_1} B_{\rho_1}^T Q_1 + \frac{1}{2} I_2 \right) \rho_{\tau_1} \\
 & + \frac{H_{1\tau}^2 - M_1^2}{\varepsilon_1} \rho_{\tau_1}^T Q_1 B_{\rho_1} B_{\rho_1}^T Q_1 \rho_{\tau_1} \\
 & + \rho_{\tau_2}^T \left(A_{\rho_2}^T Q_2 + Q_2 A_{\rho_2} + \frac{M_2^2}{\varepsilon_2} Q_2 B_{\rho_2} B_{\rho_2}^T Q_2 + \frac{1}{2} I_2 \right) \rho_{\tau_2} \\
 & + \frac{H_{2\tau}^2 - M_2^2}{\varepsilon_2} \rho_{\tau_2}^T Q_2 B_{\rho_2} B_{\rho_2}^T Q_2 \rho_{\tau_2} + \Omega
 \end{aligned} \tag{A22}$$

where the operator $\lambda_M(\cdot)$ states the maximum eigenvalue of a symmetric matrix and $\Omega = \frac{\sigma_m}{2} \theta_m^T \theta_m + \frac{\sigma_a}{2} \theta_a^T \theta_a + \frac{\sigma_P}{2} p_{21}^2 + \varepsilon_1 + \varepsilon_2$. Let $w_i > \frac{1}{2}, i = 1, 2$. According to Lemma A1, for any $k_0 > \frac{\Omega}{r} > 0$, there exist sufficiently small $\tau_i > 0, i = 1, 2$, such that the Lyapunov equation

$$\left(A_{\rho_i}^T + \frac{k_0}{2} I_2 \right) Q_i + Q_i \left(A_{\rho_i} + \frac{k_0}{2} I_2 \right) = -w_i I_2 \tag{A23}$$

possesses a positive definite solution $Q_i, i = 1, 2$. Let these matrices Q_1, Q_2 be used in the Lyapunov function.

Let us consider matrices ($i = 1, 2$)

$$R_i = A_{\rho i}^T Q_i + Q_i A_{\rho i} + \frac{M_i^2}{\varepsilon_i} Q_i B_{\rho i} B_{\rho i}^T Q_i + \frac{1}{2} I_2 + k_0 Q_i = \frac{M_i^2}{\varepsilon_i} Q_i B_{\rho i} B_{\rho i}^T Q_i - \left(w_i - \frac{1}{2} \right) I_2. \tag{A24}$$

By Lemma A1, there exists τ_{min} such that, for $\tau_i < \tau_{min} i = 1, 2$, each of the matrices R_i is negative definite, and then

$$\begin{aligned} \dot{V} \leq & -\frac{2k_a \tau_0 p_1}{J_a} \frac{J_a}{2\tau_0 p_1} e_a^2 - 2k_\psi \frac{1}{2} e_{\psi f}^2 - \frac{2k_i k_\omega}{J_m} \frac{J_m}{2k_i} e_{\omega f}^2 - \frac{\sigma_a}{2\lambda_M(\Gamma_a^{-1})} \tilde{\theta}_a^T \Gamma_a^{-1} \tilde{\theta}_a \\ & - \frac{\sigma_m}{2\lambda_M(\Gamma_m^{-1})} \tilde{\theta}_m^T \Gamma_m^{-1} \tilde{\theta}_m - \frac{\gamma_p \sigma_p}{2} \frac{1}{\gamma_p} \tilde{p}_{21}^2 - \rho_{\tau 1}^T (k_0 Q_1) \rho_{\tau 1} \\ & + \frac{H_1^2 - M_1^2}{\varepsilon_1} \rho_{\tau 1}^T Q_1 B_{\rho 1} B_{\rho 1}^T Q_1 \rho_{\tau 1} - \rho_{\tau 2}^T (k_0 Q_2) \rho_{\tau 2} \\ & + \frac{H_2^2 - M_2^2}{\varepsilon_2} \rho_{\tau 2}^T Q_2 B_{\rho 2} B_{\rho 2}^T Q_2 \rho_{\tau 2} + \Omega. \end{aligned} \tag{A25}$$

Inequality (A25) can be rewritten in the following form:

$$\dot{V} \leq -k_m V + \frac{H_1^2 - M_1^2}{\varepsilon_1} \rho_{\tau 1}^T Q_1 B_{\rho 1} B_{\rho 1}^T Q_1 \rho_{\tau 1} + \frac{H_2^2 - M_2^2}{\varepsilon_2} \rho_{\tau 2}^T Q_2 B_{\rho 2} B_{\rho 2}^T Q_2 \rho_{\tau 2} + \Omega \tag{A26}$$

where

$$k_m := \min \left\{ \frac{2k_a \tau_0 p_1}{J_a}, 2k_\psi, \frac{2k_i k_\omega}{J_m}, \frac{\sigma_a}{\lambda_M(\Gamma_a^{-1})}, \frac{\sigma_m}{\lambda_M(\Gamma_m^{-1})}, \gamma_p \sigma_p, k_0 \right\}. \tag{A27}$$

Inside the set $V(e_a, e_{\psi f}, e_{\omega f}, \tilde{\theta}_a, \tilde{\theta}_m, \tilde{p}_{21}, \rho_{\tau 1}, \rho_{\tau 2}) \leq r$, inequalities $|H_1| \leq M_1$ and $|H_2| \leq M_2$ are satisfied, and matrices $Q_i B_{\rho i} B_{\rho i}^T Q_i i = 1, 2$ are positive semi-definite. So, it follows from (A26) that

$$\dot{V} \leq -k_m V + \Omega. \tag{A28}$$

If $\frac{\Omega}{k_m} < r$, then the set

$$\mathcal{A} := \left\{ \left(e_a, e_{\psi f}, e_{\omega f}, \tilde{\theta}_a, \tilde{\theta}_m, \tilde{p}_{21}, \rho_{\tau 1}, \rho_{\tau 2} \right) : V(e_a, e_{\psi f}, e_{\omega f}, \tilde{\theta}_a, \tilde{\theta}_m, \tilde{p}_{21}, \rho_{\tau 1}, \rho_{\tau 2}) \leq \frac{\Omega}{k_m} < r \right\} \tag{A29}$$

is contained in B_1 , and any trajectory starting in B_1 is bounded and uniformly ultimately bounded to the compact set of attraction \mathcal{A} [48,49]. Therefore, this trajectory is SGUUB, according to the definition given in [47]. The set of attraction \mathcal{A} can be narrowed by a proper choice of design parameters, according to (A27) and (A29).

As the tracking error e is the response of the inertial filter with the transfer function $\frac{1}{s\tau_0+1}$ to the input e_a , it is SGUUB as e_a is, and because of the definition of e_a, \dot{e} is also bounded. Therefore, the position φ_a and velocity ω_a are bounded. As the adaptation errors $\tilde{\theta}_a, \tilde{\theta}_m, \tilde{p}_{21}$ and the exact parameters are bounded, the adaptive parameters $\hat{\theta}_a, \hat{\theta}_m, \hat{p}_{21}$ are also bounded and possess bounded derivatives.

Step by step, starting from the internal loop, the boundedness of all signals in the closed-loop system follows. The first loop stabilizing function ψ_d is bounded, and consequently, the filter state variables (16) are bounded. The next stabilizing function ω_{md} is bounded, and consequently, the second filter state variables, the motor's position and velocity and, finally, the desired current are all bounded. \square

References

1. Electric Motors and Variable Speed Drives. Available online: https://commission.europa.eu/energy-climate-change-environment/standards-tools-and-labels/products-labelling-rules-and-requirements/energy-label-and-ecodesign/energy-efficient-products/electric-motors-and-variable-speed-drives_en (accessed on 7 January 2024).
2. Peng, Y.; Cui, J.; Sun, J.; Zhang, M. Torsional Vibration for Rolling Mill with the Drive System Shaft Axis Deviations. *Arab. J. Sci. Eng.* **2021**, *46*, 12165–12177. [[CrossRef](#)]
3. Bortnowski, P.; Gładysiewicz, L.; Król, R.; Ozdoba, M. Models of Transverse Vibration in Conveyor Belt—Investigation and Analysis. *Energies* **2021**, *14*, 4153. [[CrossRef](#)]
4. Guo, Y.; Zhang, D.; Zhang, X.; Wang, S.; Ma, W. Experimental Study on the Nonlinear Dynamic Characteristics of Wire Rope under Periodic Excitation in a Friction Hoist. *Shock Vib.* **2020**, *2020*, 8506016. [[CrossRef](#)]
5. Kim, T.; Lee, U.-K.; Kim, S.W.; Lim, H.; Kim, C.-W.; Cho, H.; Kang, K.-I. Flexible Double-Cage Hoist for High Operational Efficiency in Tall Building Construction. *Autom. Constr.* **2018**, *96*, 280–291. [[CrossRef](#)]
6. Zheng, X.; Agarwal, V.; Liu, X.; Balachandran, B. Nonlinear Instabilities and Control of Drill-String Stick-Slip Vibrations with Consideration of State-Dependent Delay. *J. Sound Vib.* **2020**, *473*, 115235. [[CrossRef](#)]
7. Riane, R.; Doghmane, M.Z.; Kidouche, M.; Djezzar, S. Observer-Based H_∞ Controller Design for High Frequency Stick-Slip Vibrations Mitigation in Drill-String of Rotary Drilling Systems. *Vibration* **2022**, *5*, 264–289. [[CrossRef](#)]
8. Chang, R.-I.; Lee, C.-Y.; Hung, Y.-H. Cloud-Based Analytics Module for Predictive Maintenance of the Textile Manufacturing Process. *Appl. Sci.* **2021**, *11*, 9945. [[CrossRef](#)]
9. Valenzuela, M.A.; Bentley, J.M.; Lorenz, R.D. Evaluation of Torsional Oscillations in Paper Machine Sections. *IEEE Trans. Ind. Appl.* **2005**, *41*, 493–501. [[CrossRef](#)]
10. Heikkinen, J.E.; Ghalamchi, B.; Viitala, R.; Sopanen, J.; Juhanko, J.; Mikkola, A.; Kuosmanen, P. Vibration Analysis of Paper Machine's Asymmetric Tube Roll Supported by Spherical Roller Bearings. *Mech. Syst. Signal Process.* **2018**, *104*, 688–704. [[CrossRef](#)]
11. Lu, G.; Zhou, J.; Cai, G.; Lv, L.; Fang, G. Active Vibration Control of a Large Space Antenna Structure Using Cable Actuator. *AIAA J.* **2021**, *59*, 1457–1468. [[CrossRef](#)]
12. Liu, X.; Zhang, H.; Lv, L.; Peng, F.; Cai, G. Vibration Control of a Membrane Antenna Structure Using Cable Actuators. *J. Frankl. Inst.* **2018**, *355*, 2424–2435. [[CrossRef](#)]
13. Zhang, Y.; Zhang, M.; Fan, C.; Li, F. A Finite-Time Trajectory-Tracking Method for State-Constrained Flexible Manipulators Based on Improved Back-Stepping Control. *Actuators* **2022**, *11*, 139. [[CrossRef](#)]
14. Nanos, K.; Papadopoulos, E.G. On the Dynamics and Control of Flexible Joint Space Manipulators. *Control Eng. Pract.* **2015**, *45*, 230–243. [[CrossRef](#)]
15. Yang, H.; Wang, Z.; Zhang, T.; Du, F. A Review on Vibration Analysis and Control of Machine Tool Feed Drive Systems. *Int. J. Adv. Manuf. Technol.* **2020**, *107*, 503–525. [[CrossRef](#)]
16. Awada, A.; Younes, R.; Ilinca, A. Review of Vibration Control Methods for Wind Turbines. *Energies* **2021**, *14*, 3058. [[CrossRef](#)]
17. Hua, Y.; Wang, S.; Li, B.; Bai, G.; Zhang, P. Dynamic Modeling and Anti-Disturbing Control of an Electromagnetic MEMS Torsional Micromirror Considering External Vibrations in Vehicular LiDAR. *Micromachines* **2021**, *12*, 69. [[CrossRef](#)]
18. Wang, C.; Liu, J.; Xin, L.; Li, G.; Pan, J. Design of Full-Order State Observer for Two-Mass Joint Servo System Based on the Fixed Gain Filter. *IEEE Trans. Power Electron.* **2022**, *37*, 10466–10475. [[CrossRef](#)]
19. Li, W.; Chen, L. Study on Modeling and Degradation Law of Transmission Efficiency for Harmonic Reducer. *J. Fail. Anal. Prev.* **2022**, *22*, 1943–1953. [[CrossRef](#)]
20. Zhang, X.; Liu, H.; Zhan, Z.; Wu, Y.; Zhang, W.; Taha, M.; Yan, P. Modelling and Active Damping of Engine Torque Ripple in a Power-Split Hybrid Electric Vehicle. *Control Eng. Pract.* **2020**, *104*, 104634. [[CrossRef](#)]
21. Liu, H.; Zhang, X.; Chen, Y.; Taha, M.; Xu, H. Active Damping of Driveline Vibration in Power-Split Hybrid Vehicles Based on Model Reference Control. *Control Eng. Pract.* **2019**, *91*, 104085. [[CrossRef](#)]
22. De Luca Alessandro and Book, W.J. Robots with Flexible Elements. In *Springer Handbook of Robotics*; Bruno, S., Khatib, O., Eds.; Springer International Publishing: Cham, Switzerland, 2016; pp. 243–282. ISBN 978-3-319-32552-1.
23. Lu, Y.; Yang, Y.; Xue, Y.; Jiang, J.; Zhang, Q.; Yue, H. A Variable Stiffness Actuator Based on Leaf Springs: Design, Model and Analysis. *Actuators* **2022**, *11*, 282. [[CrossRef](#)]
24. Misgeld, B.J.E.; Hewing, L.; Liu, L.; Leonhardt, S. Closed-Loop Positive Real Optimal Control of Variable Stiffness Actuators. *Control Eng. Pract.* **2019**, *82*, 142–150. [[CrossRef](#)]
25. Jonathan, H.; Green, K. Series Elastic Actuation. In *Encyclopedia of Robotics*; Ang Marcelo, H., Khatib, O.S.B., Eds.; Springer: Berlin/Heidelberg, Germany, 2020; pp. 1–12. ISBN 978-3-642-41610-1.
26. Szabat, K.; Orłowska-Kowalska, T. Vibration Suppression in a Two-Mass Drive System Using PI Speed Controller and Additional Feedbacks—Comparative Study. *IEEE Trans. Ind. Electron.* **2007**, *54*, 1193–1206. [[CrossRef](#)]
27. Orłowska-Kowalska, T.; Dybkowski, M.; Szabat, K. Adaptive Sliding-Mode Neuro-Fuzzy Control of the Two-Mass Induction Motor Drive without Mechanical Sensors. *IEEE Trans. Ind. Electron.* **2010**, *57*, 553–564. [[CrossRef](#)]
28. Serkies, P.J.; Szabat, K. Application of the MPC to the Position Control of the Two-Mass Drive System. *IEEE Trans. Ind. Electron.* **2013**, *60*, 3679–3688. [[CrossRef](#)]

29. Yakub, F.; Mori, Y. Intelligent Control Method for Two-Mass Rotary Positioning Systems. In Proceedings of the SICE Annual Conference 2013, Nagoya, Japan, 14–17 September 2013; pp. 2524–2529.
30. Kamiński, M.; Szabat, K. Adaptive Control Structure with Neural Data Processing Applied for Electrical Drive with Elastic Shaft. *Energies* **2021**, *14*, 3389. [[CrossRef](#)]
31. Shang, D.; Li, X.; Yin, M.; Li, F. Dynamic Modeling and Control for Dual-Flexible Servo System Considering Two-Dimensional Deformation Based on Neural Network Compensation. *Mech. Mach. Theory* **2022**, *175*, 104954. [[CrossRef](#)]
32. Kabziński, J.; Mosiołek, P. Adaptive Control of Nonlinear Resonant Systems with Damping. In Proceedings of the 2015 20th International Conference on Methods and Models in Automation and Robotics, MMAR, Miedzyzdroje, Poland, 24–27 August 2015; pp. 659–664.
33. Kabziński, J. Adaptive Control of Drillstring Torsional Oscillations. *IFAC-PapersOnLine* **2017**, *50*, 13360–13365. [[CrossRef](#)]
34. Kabziński, J. Oscillations and Friction Compensation in Two-Mass Drive System with Flexible Shaft by Command Filtered Adaptive Backstepping. *IFAC-PapersOnLine* **2015**, *48*, 307–312. [[CrossRef](#)]
35. Inoue, Y.; Katsura, S. Spatial Disturbance Suppression of a Flexible System Based on Wave Model. *IEEJ J. Ind. Appl.* **2018**, *7*, 236–243. [[CrossRef](#)]
36. Assanimoghaddam, M.; Acquatella, B.P. Algebraic Estimation and Control of Single-Link Flexible Joint Robots. In Proceedings of the 2017 IEEE/RSJ International Conference on Intelligent Robots and Systems (IROS), Vancouver, BC, Canada, 24–28 September 2017; pp. 1657–1663.
37. Diao, S.; Sun, W.; Su, S.-F.; Zhao, X.; Xu, N. Novel Adaptive Control for Flexible-Joint Robots with Unknown Measurement Sensitivity. *IEEE Trans. Autom. Sci. Eng.* **2023**, 1–12. [[CrossRef](#)]
38. Zhang, Q.; Liu, X.; Cai, G. Dynamics and Control of a Flexible-Link Flexible-Joint Space Robot with Joint Friction. *Int. J. Aeronaut. Space Sci.* **2021**, *22*, 415–432. [[CrossRef](#)]
39. Kabziński, J.; Mosiołek, P. Observer-Based, Robust Position Tracking in Two-Mass Drive System. *Energies* **2022**, *15*, 9093. [[CrossRef](#)]
40. Kabziński, J.; Mosiołek, P. Integrated, Multi-Approach, Adaptive Control of Two-Mass Drive with Nonlinear Damping and Stiffness. *Energies* **2021**, *14*, 5475. [[CrossRef](#)]
41. Liu, H.; Cui, S.; Liu, Y.; Ren, Y.; Sun, Y. Design and Vibration Suppression Control of a Modular Elastic Joint. *Sensors* **2018**, *18*, 1869. [[CrossRef](#)] [[PubMed](#)]
42. Yuki, K.; Murakami, T.; Ohnishi, K. Vibration Control of 2 Mass Resonant System by Resonance Ratio Control. In Proceedings of the IECON '93—19th Annual Conference of IEEE Industrial Electronics, Maui, HI, USA, 15–19 November 1993; Volume 3, pp. 2009–2014.
43. di Meglio, F.; Aarsnes, U.J.F. A Distributed Parameter Systems View of Control Problems in Drilling. *IFAC Proc. Vol. (IFAC-PapersOnLine)* **2015**, *48*, 272–278. [[CrossRef](#)]
44. Saldivar, B.; Mondié, S.; Ávila Vilchis, J.C. The Control of Drilling Vibrations: A Coupled PDE-ODE Modeling Approach. *Int. J. Appl. Math. Comput. Sci.* **2016**, *26*, 335–349. [[CrossRef](#)]
45. Saldivar, B.; Mondie, S.; Loiseau, J.J.; Rasvan, V. Stick-Slip Oscillations in Oilwell Drillstrings: Distributed Parameter and Neutral Type Retarded Model Approaches. *IFAC Proc. Vol.* **2011**, *18*, 284–289. [[CrossRef](#)]
46. Boussaada, I.; Mounier, H.; Niculescu, S.I.; Cella, A. Analysis of Drilling Vibrations: A Time-Delay System Approach. In Proceedings of the 2012 20th Mediterranean Conference on Control and Automation, MED 2012—Conference Proceedings, Barcelona, Spain, 3–6 July 2012; pp. 610–614.
47. Zhao, X.; Wang, X.; Zong, G.; Li, H. Fuzzy-Approximation-Based Adaptive Output-Feedback Control for Uncertain Nonsmooth Nonlinear Systems. *IEEE Trans. Fuzzy Syst.* **2018**, *26*, 3847–3859. [[CrossRef](#)]
48. Kabziński, J.; Mosiołek, P.W.N. *Projektowanie Nieliniowych Układów Sterowania*; Monografie—Komitet Automatyki i Robotyki Polskiej Akademii Nauk; Wydawnictwo Naukowe PWN SA: Warsaw, Poland, 2018; ISBN 9788301196974.
49. Khalil, H.K. *Nonlinear Systems*; Pearson Education; Prentice Hall: Upper Saddle River, NJ, USA, 2002; ISBN 9780130673893.

Disclaimer/Publisher's Note: The statements, opinions and data contained in all publications are solely those of the individual author(s) and contributor(s) and not of MDPI and/or the editor(s). MDPI and/or the editor(s) disclaim responsibility for any injury to people or property resulting from any ideas, methods, instructions or products referred to in the content.